Electrical coupling regulated by GABAergic nucleo-olivary afferent fibres facilitates cerebellar sensory–motor adaptation

Niceto R. Luque [a,b,*], Francisco Naveros [b,c], Ignacio Abadía [b], Eduardo Ros [b,1], Angelo Arleo [a,1]

[a] *Sorbonne Université, INSERM, CNRS, Institut de la Vision, 17 rue Moreau, F-75012 Paris, France*
[b] *Department of Computer Architecture and Technology, CITIC-University of Granada, 2 Calle Periodista Rafael Gómez Montero, ES 18014 Granada, Spain*
[c] *Department of Neuroscience, Baylor College of Medicine, Houston, TX, USA*

ABSTRACT

The inferior olivary (IO) nucleus makes up the signal gateway for several organs to the cerebellar cortex. Located within the sensory–motor-cerebellum pathway, the IO axons, i.e., climbing fibres (CFs), massively synapse onto the cerebellar Purkinje cells (PCs) regulating motor learning whilst the olivary nucleus receives negative feedback through the GABAergic nucleo-olivary (NO) pathway. The NO pathway regulates the electrical coupling (EC) amongst the olivary cells thus facilitating synchrony and timing. However, the involvement of this EC regulation on cerebellar adaptive behaviour is still under debate. In our study we have used a spiking cerebellar model to assess the role of the NO pathway in regulating vestibulo-ocular-reflex (VOR) adaptation. The model incorporates spike-based synaptic plasticity at multiple cerebellar sites and an electrically-coupled olivary system. The olivary system plays a central role in regulating the CF spike-firing patterns that drive the PCs, whose axons ultimately shape the cerebellar output. Our results suggest that a systematic GABAergic NO deactivation decreases the spatio-temporal complexity of the IO firing patterns thereby worsening the temporal resolution of the olivary system. Conversely, properly coded IO spatio-temporal firing patterns, thanks to NO modulation, finely shape the balance between long-term depression and potentiation, which optimises VOR adaptation. Significantly, the NO connectivity pattern constrained to the same micro-zone helps maintain the spatio-temporal complexity of the IO firing patterns through time. Moreover, the temporal alignment between the latencies found in the NO fibres and the sensory–motor pathway delay appears to be crucial for facilitating the VOR. When we consider all the above points we believe that these results predict that the NO pathway is instrumental in modulating the olivary coupling and relevant to VOR adaptation.

1. Introduction

The vestibulo-ocular-reflex (VOR) is a reflex of the eye movement that stabilises the images on the retina during head movements by producing contralateral eye movements that maintain the image in the centre of the visual field. During rotational VOR, the vestibular system senses head rotation signals that are later processed in the vestibular nuclei and cerebellum to stabilise the eyes (Fig. 1A). The cerebellum and the vestibular nuclei are reciprocally inter-connected (Lorente de Nó, 1933). The vestibular nuclei outputs (efferent) are directly connected to the cerebellum via the mossy fibres–granule cells (MF–GrC) and indirectly via the inferior olivary cells (IO). The IO, in turn, is the sole source of climbing fibres (CFs), conveying the teaching signal and targeting the Purkinje cells (PCs) in the cerebellar cortex. PCs integrate both the activity from the parallel fibres (PFs, i.e., GrC axons) and the teaching signal from the olivo-cerebellar projections (retinal slips) and they send inhibitory axons to the medial vestibular nuclei (MVN) (Ito, 2002). This circuitry is pivotal for VOR adaptation by means of distributed plasticity at GrC–PC and MF–MVN synapses where the adaptation mechanisms are driven by CF and PC activity respectively (Badura et al., 2016; Clopath et al., 2014; Luque et al., 2019, 2022) (Fig. 1B). There is a large body of research on the computation of the vestibular information at the vestibular nuclei and cerebellum, however, the role of the

* Corresponding author at: Department of Computer Architecture and Technology, CITIC-University of Granada, 2 Calle Periodista Rafael Gómez Montero, ES 18014 Granada, Spain.
E-mail addresses: nluque@ugr.es (N.R. Luque), fnaveros@ugr.es (F. Naveros), iabadia@ugr.es (I. Abadía), eros@ugr.es (E. Ros), angelo.arleo@inserm.fr (A. Arleo).
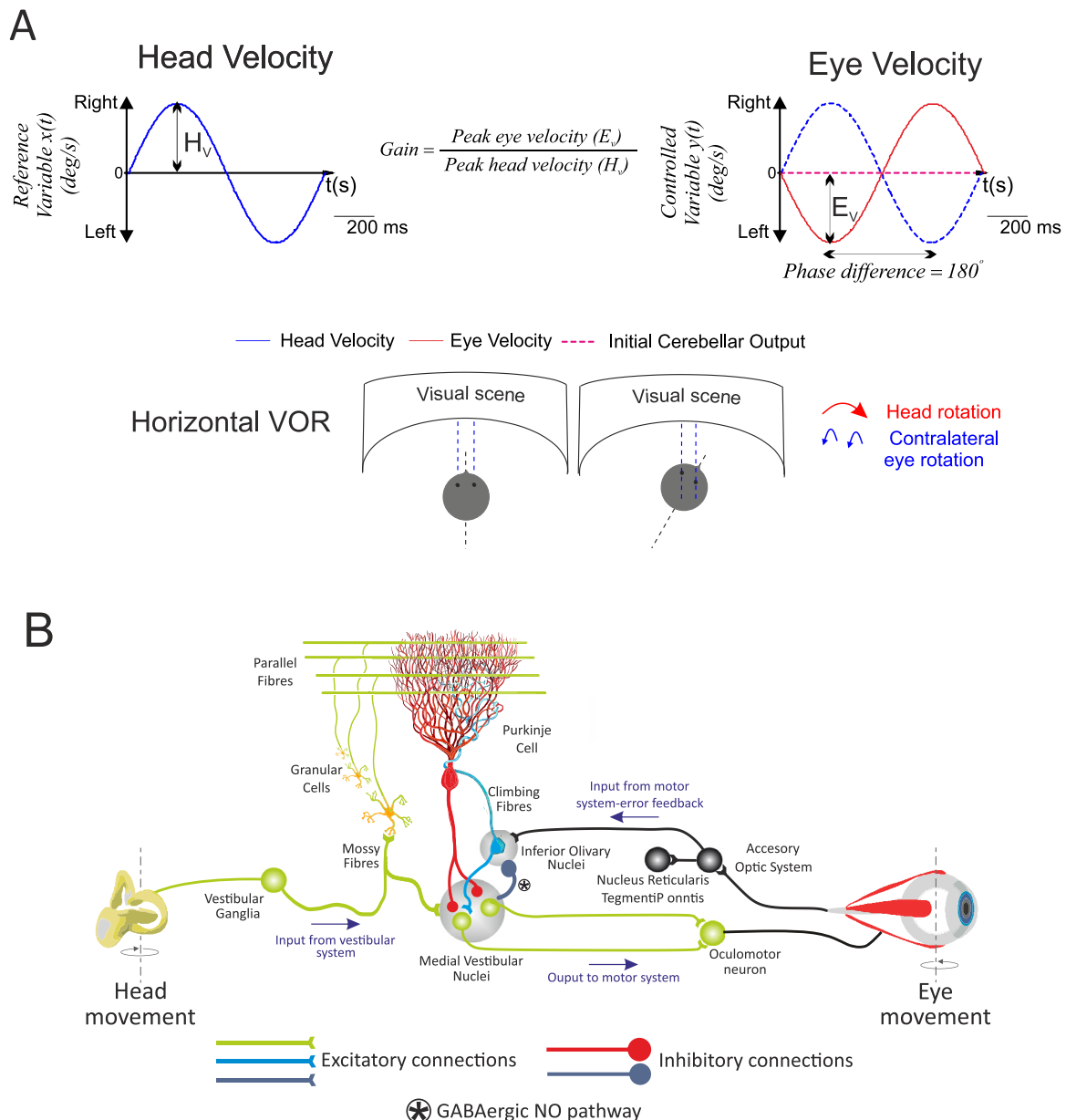[1] AA and ER are Joint Senior Authors.

Fig. 1. Vestibular Ocular Reflex (VOR) and cerebellar control loop. **(A)** Horizontal VOR (h-VOR) protocols compare head rotational movements (input) against the induced contralateral eye movements (output) via two measurements: the VOR gain, i.e., the ratio between eye and head speeds (E_v and H_v, respectively); and the VOR phase, i.e., the temporal lag between eye and head velocity signals. The head velocity consists of a 1 Hz sinusoidal function iteratively presented to the cerebellar model, mimicking the sinusoidal frequency of the head rotation in experimental protocols (Leigh & Zee, 2015). **(B)** Schematic representation of the main neural layers, cells, connections and plasticity sites considered in the cerebellar model. Mossy fibres (MFs) convey the sensory signals from the vestibular organ and they provide the input to the cerebellar network. MFs project sensory–motor information onto granular cells (GrCs) and medial vestibular nuclei (MVN). GrCs, in turn, project onto Purkinje cells (PCs) through parallel fibres (PFs). The PCs also receive excitatory inputs from the climbing fibres (CFs). CFs deliver the error signals encoding instructive terms that drive motor control learning. The PCs integrate CF and PF inputs, thus transmitting the difference between head and eye movements. Finally, MVN cells receive inhibitory afferents from PCs and excitatory afferents from the CFs. The MVN closes the CF–PC–MVN loop via the GABAergic projections onto the IO network and provides the main cerebellar output. The cerebellar model implements different spike timing dependent plasticity mechanisms at PF–PC and MF–MVN synapses. (For interpretation of the references to colour in this figure legend, the reader is referred to the web version of this article.)

olivary system in processing the vestibular information during VOR adaptation has scarcely been studied (Li et al., 2013).

The olivary system provides powerful excitatory inputs to the PCs and induces long-term plasticity changes whilst it is responding to natural stimulations of the vestibular system during vestibular-related motor learning. Simultaneously, the vestibular-related GABAergic projections from the vestibular nucleus, i.e., the parasolitary nucleus (Barmack et al., 1998; Li et al., 2013) are conveyed to the IO, i.e., sub-nucleus (IOb) (Barmack et al., 1998; Li et al., 2013). The NO axon pathway conformed by the GABAergic projections to the IO ends at the IO glomeruli,

through which neighbouring IO neurons are coupled via electrical synapses formed by gap junctions (GJs). These GABAergic synaptic inputs, together with glutamatergic inputs (Turecek & Regehr, 2020), are critical for the regulation of the electrical coupling (EC) strength between the IO neurons (Lefler et al., 2014), i.e., the GJ conductance is unaltered whereas the GJ current is shunted. Coupling or uncoupling the IO neurons by modulating their electrical synaptic strength affects the synchronicity of IO activity, which has a direct impact on cerebellar adaptation.

IO neurons are thought to convey the teaching signal via CFs typically firing at a very low rate (1–10 Hz). The low firing

rate compromises the temporal resolution of the teaching signal of single cells thus limiting its timing-precision. However, the IO connectivity and its probabilistic Poisson process activation is hypothesised to mitigate this problem (Carrillo et al., 2008; Luque et al., 2019, 2022). IO neurons operate in ensembles and their synchronicity regulates the associated PC neuronal population downstream which drives the MVN output and ultimately activates the eye motor neurons during VOR. An entire olivary-system that is operating synchronously denotes IO activations in ensembles as if they were acting as a single neuron. Consequently, the number of joint neuron activities constituting the population coding of the teaching signal decreases (Schneidman, 2016), as well as the IO temporal resolution. Nonetheless, asynchronous IO activations indicate a sparse spike-time generation, which increases the time resolution of the population coding of the teaching signal. The modulation of the dendro–dendritic GJs, which interconnect the olivary neurons, regulates the level of IO synchrony; a rather strong or weak coupling strength induces single neuron dynamics whereas intermediate coupling strength induces desynchronised IO activities that help optimise population coding (Schweighofer et al., 2004). Anatomical evidence suggests that electrically-coupled IO neurons are partially driven by the MVN inhibitory projections onto IO neurons. The small MVN GABAergic neurons inhibit the IO and regulate the formation of IO synchronous firing and their coupling (Lefler et al., 2014; Najac & Raman, 2015). However, the impact of these nuclei GABAergic synaptic inputs on the IO spatial coding capability during VOR cerebellar adaptation is not yet fully understood (Best & Regehr, 2009; Llinas et al., 1974; Uusisaari & De Schutter, 2011).

Kawato et al. (2011) and Tokuda et al. (2013) proposed the closed-loop neural circuit conformed by IOs, PCs, and cerebellar nuclei (CN, equivalent to the MVN role) as having a functional role in changing the IO coupling strength during cerebellar motor learning. Presumably, the presence of large teaching signals at early stages of motor learning drives large PC activations and the subsequent suppression of CN cells (Kawato et al., 2011). Consequently, the suppressed CN cells deactivate their inhibitory shunting effects on the olivary GJs thus allowing the strong EC. Conversely, the later stages of motor learning involve weak teaching signals that cause weak PC activations, weak CN suppressions and a CN firing-rate increase. The strong inhibitory shunting effects of CNs onto GJs produce weak EC within the olivary system. Despite the smart explanation provided by Kawato et al. about the electrical coupling modulation there are still key questions to be tackled.

Experimental evidence shows that a spike in the CF efferent to a PC is more likely to depress a PF–PC synapse via long-term depression (LTD) if the corresponding PF fired prior to the IO spike arrival to the PC through the CFs, i.e., ~ 100 ms before (Kettner et al., 1997; Luque et al., 2016; Raymond & Lisberger, 1998; Suvrathan et al., 2016). If so, initial strong teaching signals through CFs would drive weak PF–PC synapse activations, and simultaneously strong MVN activations via the CF–MVN collateral connections (Luque et al., 2014). Therefore, decreasingly activated PCs, even at initial VOR learning stages, would generate a subsequent weak inhibition to the MVN that may eventually cause a synaptic counter effect to coupling which strengthens at the IO, in contrast to Kawato's hypothesis. This counter effect at initial VOR learning stages may even be amplified by the MF–MVN synaptic depression produced when a spike from the PC efferent fibre reaches a target MVN (Luque et al., 2016, 2019, 2022), the MVN activations via CF collaterals (Luque et al., 2014), and the gating mechanism mediated by PC spike burst-pause sequences that cause an early and coarse VOR adaptation (Luque et al., 2019).

Moreover, the long latency of the inhibition elicited by direct stimulation of the NO pathway is intriguing. The peak inhibition at the IO occurs after about 35–50 ms in cats (the larger

the species, the greater the delay) (Hesslow, 1986; Svensson et al., 2006) and it desynchronises the teaching signal from the MVN inhibitory shunting on the olivary GJs. Another fundamental question is whether the olivary–nuclei–olivary loop is preserved. That is, whether the MVN neuron that is receiving cortical inhibition exclusively from a PC driven by a certain IO is closing the loop through that particular IO. The final piece of the puzzle comes from the additional modulation of the MVN by the excitatory olivary CF collaterals. These CF collaterals are mainly localised in the ventral part of the lateral MVN closely related to the flocculus, a cerebellar region that plays a fundamental role in vestibulo-ocular functions (Uusisaari & De Schutter, 2011). In this study we have built upon, deepened, and addressed these fundamental questions via a horizontal–VOR (h–VOR) closed-loop set-up by using a spiking cerebellar model at the core of the vestibular adaptation.

2. Results

We first characterised the EC within an olivary system in isolation and verified that specific activations of its GABAergic inputs (i.e., NO axons), reduced the coupling coefficient (CC) amongst IOs (see Methods). This reduction varies with the coupling distance: linearly under negative injected currents and exponentially under positive injected currents to the central IO (see Supplementary Figs. S1 & S2). After the EC characterisation, we inserted our olivary system within a cerebellar spiking network located at the core of a feed forward controller acting during h–VOR adaptation. We determined that the exponential CC reduction via the NO pathway facilitated desynchronising the CF spike generation during cerebellar learning, as otherwise the accuracy and learning consolidation during h – VOR (Figs. S3 & S4) would be compromised (Section 2.1, Figs. 2 & 3, and Fig. S5). Our results also suggest that not only the GABAergic NO action, but also the NO pathway topology in closing the olivo-cortico-nucleo-olivary (OCNO) loop, are key in desynchronising the CF spike generation within the same micro-complex (Section 2.2, Fig. 4, and Figs. S6 & S7) during h–VOR adaptation. The NO pathway topology was also found to be relevant in allowing single neuron olivary dynamics under GABAergic NO activations at initial adaptation stages (Section 2.2, Fig. S8). Interestingly, we found a beneficial timing correspondence between the long latency of the NO pathway and the sensory–motor pathway delay (~ 100 ms). The temporal alignment of the teaching signal with its neural consequences enhanced h–VOR performance (Section 2.3, Fig. 5, and Fig. S9). Concurrently, we verified a two-fold role of the complementary olivary–nuclei path (IO–MVN) during h-VOR adaptation; (i) providing a coarse but prompt MVN synaptic response to the signalled error, (ii) adjusting the MVN temporal activation better to finely shape the subsequent neural drive motor commands (Section 2.4, Figs. 6 & 7).

2.1. Nucleo-olivary axons mediate coupling strength during VOR adaptation

The idea of an IO coupling modulation via NO GABA projections was applied to an h-VOR adaption set-up. We assessed h-VOR adaptation using a spiking cerebellar model able to compensate for 1 Hz horizontal head rotations by contralateral eye movements. We tested the role of the IO coupling modulation under GABAergic NO de/activations with plasticity engaged across certain cerebellar projections for 1000 s (see long-term potentiation/long-term depression LTP/LTD sensitivity analysis carried out in Figs. S3 & S4). The CF input driving the PCs downstream was taken to signal large retinal slips, which generated sequences of graded complex spikes made of 2 to 5 burst spikelets
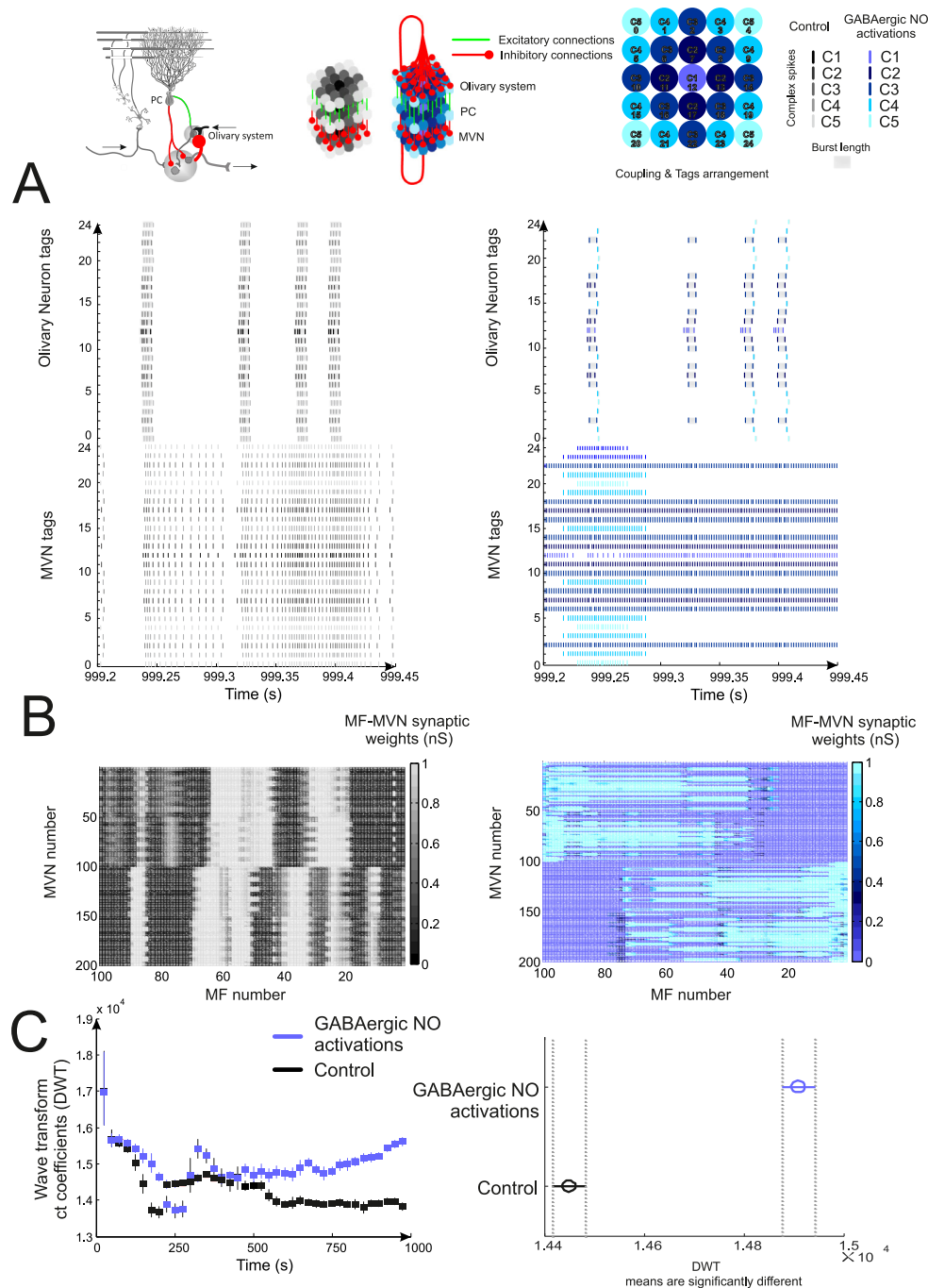
Fig. 2. Nucleo-olivary pathway de/activations during VOR adaptation. The diagram depicts a schematic representation of the main cells and synaptic connections recorded during h-VOR adaptation (1 Hz h-VOR during 1000 s). **(A)** The CF input driving Purkinje cells signals drove large retinal slips that generated sequences of complex spikes made of 2 to 5 burst spikelet depending on the amplitude of the signalled error. GABAergic NO deactivations cause synchronisation in the sequences of complex spikes (left panel); the firing rate amongst CFs remains constant due to the lack of IO electrical coupling modulation provided by GABAergic olivary afferents. IO neurons are activated as if they were a single neuron; there is no neural specificity for the olivary-neural coding (all-or-nothing codification). GABAergic NO activations during h-VOR adaptation cause desynchronisation in the sequences of complex spikes (right panel). The firing rate amongst CFs (i.e., IO axons) decreased exponentially with the coupling distance to central olivary neuron (Fig. S2). MVN activations after h-VOR adaptation reflected how the lack of temporal diversity of the olivary-neural coding under GABAergic NO deactivations affects the IO–PC–MVN loop. MVN activations lack temporal diversity as occurs with the IOs to which the MVN are connected (directly and indirectly through their corresponding PC). See Figure S5 for and extended snapshot. **(B)** The correlation between MF and PC activity under GABAergic NO activations are made almost afferent-to-afferent whereas GABAergic NO deactivations force this correlation to be afferent set-to-afferent set (grey (control) vs. blue synaptic weights). Flat coloured surfaces indicate low synaptic weight granularity and afferent specificity, i.e., equal synaptic weight values. **(C)** Synaptic weight values during h–VOR adaptation plotted as a sequence of images to which the DWT transform (Latorre et al., 2013) was applied. Each image (Fig. 2B) depicts the MF–MVN synaptic weight distribution at each VOR trial (all-to-one connectivity pattern, see Table 1) from 0 to 1000 s, i.e., 1000 images. Figure C left depicts the average and standard deviation of the DWT coefficients obtained each 25 s period (25 images) during h–VOR adaptation (1000 s). Figure C right depicts a multiple comparison post hoc test across the DWT curves (values) obtained during h–VOR adaptation. Statistically significant differences were found between DWT curves (ANOVA $F_{(1,1948)}$ = 193, p < 10^{-40}). The number of DWT coefficients quantifies the degree of granularity of MF – MVN synapses during h–VOR adaptation. The more intricate the synaptic weight images, the higher the number of DWT coefficients and thus the granularity. GABAergic NO activations help maintain MF – MVN synaptic weight granularity higher during h–VOR adaptation. (For interpretation of the references to colour in this figure legend, the reader is referred to the web version of this article.)
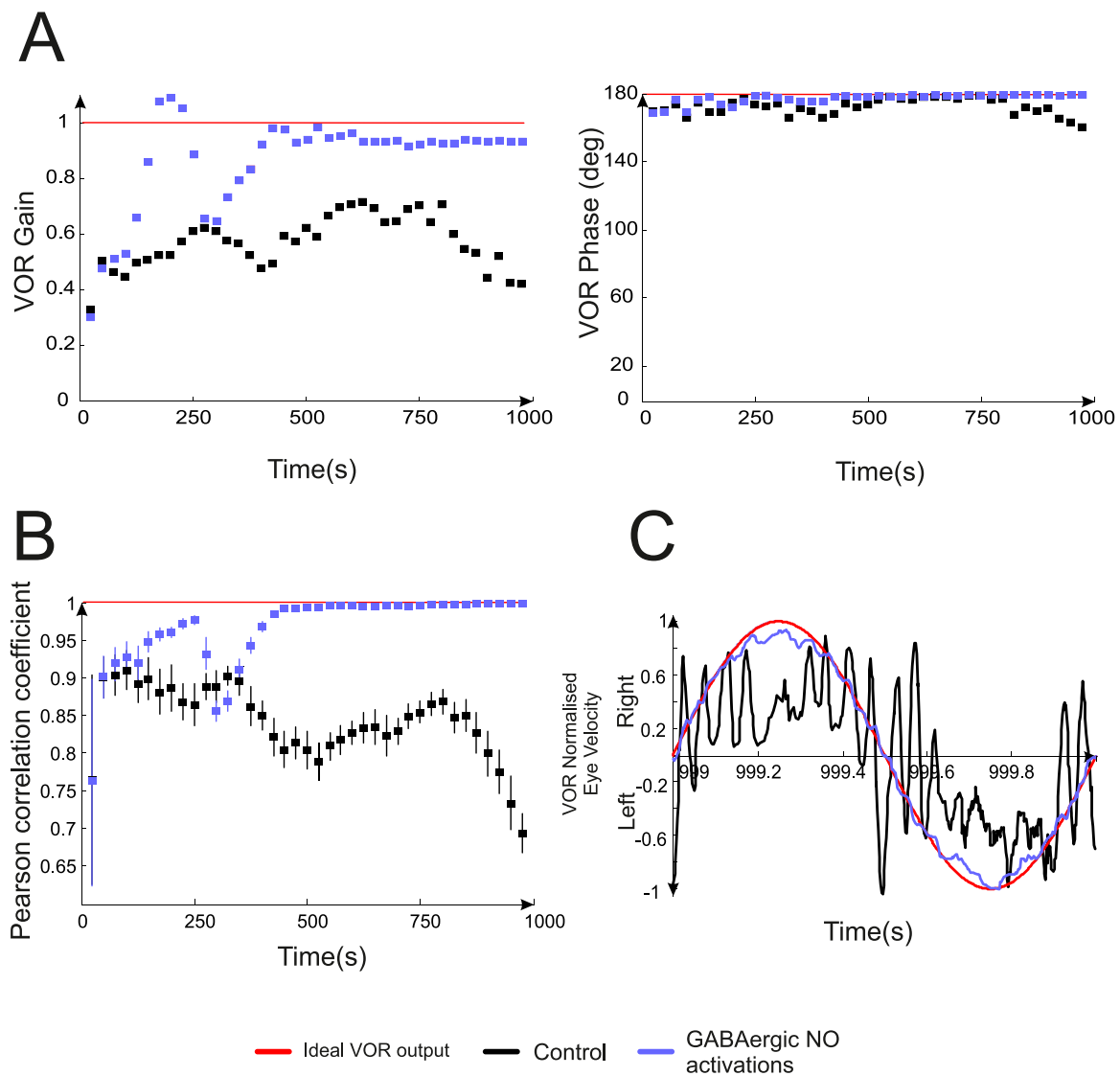
Fig. 3. Nucleo-olivary path activations facilitate VOR adaptation. **(A)** VOR gain and phase adaptation under GABAergic NO activations (purple curve) and under GABAergic NO deactivations (grey curve) during VOR adaptation (1 Hz h-VOR during 1000 s). VOR cerebellar adaptation starts with zero gain owing to the initial synaptic weights at MF–MVN afferents (Table 1). GABAergic NO activation provides better VOR gain adaptation and phase (in terms of both rate and precision) converging to values within [0.85–0.95] (see Fig. S3 & S4, LTP/LTD sensitivity analysis), which is consistent with experimental data (Minor & Goldberg, 1991; Van Alphen et al., 2001; Williams et al., 2007). **(B)** Pearson's coefficient unifies VOR gain and phase in a one dimensional measurement. **(C)** Eye velocity after VOR adaptation (1 Hz h-VOR during 1000 s); ideal (red curve) under GABAergic NO activations (purple curve), and under GABAergic NO deactivations (grey curve). (For interpretation of the references to colour in this figure legend, the reader is referred to the web version of this article.)

(Najafi & Medina, 2013) depending on the sensed retinal slip amplitude. The subsequent PC complex spike sequences (Luque et al., 2019, 2022) shaped the temporal disinhibition of the targeted MVN neurons, thus allowing the incoming input from MFs to drive the MVN responses, which in turn modulated the IO electrical coupling. IO, PCs, and MVN cells were clustered into two micro complexes (Apps & Hawkes, 2009; Ito, 1984, 2002; Marshall & Lang, 2009), making up a closed loop network (see Methods). Each micro-complex compensated for either clockwise or anticlockwise head movements by driving the corresponding agonist or antagonist eye motor neuron.

A comparison of the VOR adaptation accuracy under either GABAergic NO de/activations, done experimentally by using GABA-blocker bicuculline (Bengtsson & Hesslow, 2006), showed that the GABAergic NO inputs facilitated: (i) a better temporal resolution of the olivary system (see Fig. 2A, Fig. S5 and the spike coherence measurements below), (ii) a higher variability at MF–MVN synaptic weights (Fig. 2B) and (iii) a more complex evolution of the spatio-temporal patterns (Fig. 2C).

The evolution of the spatio-temporal neural patterns at MF–MVN synapses was characterised with the Discrete Wavelet Transform (DWT) (Latorre et al., 2013). DWT considered these patterns as a sequence of images representing the synaptic weight evolution of MF–MVN synapses where the compression rate was calculated, i.e., the number of DWT coefficients per image. The evolution of the spatio-temporal pattern complexity was therefore translated into a one-dimensional temporal signal. A higher value for DWT coefficients indicated a rather complex spatial structure for the MF–MVN synaptic weights during the VOR adaptation process (1000 s). A more complex spatial structure was facilitated by GABAergic NO activations (Fig. 2C, final DWT coefficients = $1.38 \cdot 10^4$ vs $1.56 \cdot 10^4$ GABAergic NO de/activations). A lower number of DWT coefficients during VOR adaptation indicated a uniform space amongst the sequence of MF–MVN synaptic weight images (Fig. 2C, black line). The PC axons remained more active and synchronised by saturating up or down MF–MVN synapses (Fig. 2B). The black and white coloured

flat surfaces in Fig. 2B indicated a lower variability at MF–MVN synaptic weights under GABAergic NO deactivations. Conversely, GABAergic NO activations allowed for a higher IO activation variability as depicted in Fig. 2A. A higher level of granularity with regard to MF–MVN synaptic weights (Fig. 2A, right) indicated that all the PC activations differed substantially. These PC activations resulted directly from the olivary action driving the spike-timing dependent plasticity (STDP) at the PF–PC synapses. Synchronous PC activations pointed directly to synchronously received CF signals from the IO under GABAergic NO deactivations. Coherence measures (CM) compared the spike trains elicited by the MVN connected directly to IO_{C1} and indirectly via a PC, to spike trains elicited by MVNs connected to IOs at C2, C3, C4, and C5 after h-VOR adaptation. The last 100 s of the learning process offered an almost spike invariant behaviour that allowed MVN coherence measures to be calculated. We obtained CM values near or equal to zero under GABAergic NO activations indicating upstream olivary desynchronisation ($CM_{C1-C2} = 0.3958$, $CM_{C1-C3} = 0$, $CM_{C1-C4} = 0$, $CM_{C1-C5} = 0$), whereas greater and different to zero CM values indicated a certain degree of olivary synchronisation under GABAergic NO deactivations ($CM_{C1-C2} = 0.7684$, $CM_{C1-C3} = 0.2074$, $CM_{C1-C4} = 0.1325$, $CM_{C1-C5} = 0.0916$).

VOR gain converged to a plateau of ∼0.95 gain (Fig. 3A, left) and 180° phase (Fig. 3A, right, Fig. S3 & S4) under GABAergic NO activations, which is consistent with experimental recordings in mice (Van Alphen et al., 2001), monkeys (Minor & Goldberg, 1991), and humans (Williams et al., 2007). Conversely, under GABAergic NO deactivations, the VOR gain reaches values below 0.7 (Fig. 3A, left, Figs. S3 & S4). We used the Pearson correlation coefficient to measure the similarity between head and eye velocity as if the VOR gain and phase were combined in a single value. The Pearson correlation coefficient indicated that the GABAergic NO activations facilitated VOR adaptation convergence (PCC ∼1.000 ± 0.0001 vs. PCC = 0.746 ± 0.020, Fig. 3B) obtaining a nearly perfect counteracting eye-velocity curve (Fig. 3C). The GABAergic NO deactivations caused velocity overshoots in the counteracting eye-velocity curve (Fig. 3C) indicating repeated synchronous activations of the PC axons upstream. Synchronous PC activations were driven by a synchronous olivary system that was lacking electrical coupling regulation, i.e., the neuron populations were acting as if they were a single on/off IO cell.

2.2. Closing the IO–PC–MVN loop, NO pattern connectivity is critical in VOR adaptation

The cerebellar spiking model clustered the IO, PC, and MVN cells into two micro-complexes compensating for either clockwise or anti-clockwise head movements. We tested the influence of the connectivity pattern through which the OCNO loop (Luque et al., 2022; Uusisaari & De Schutter, 2011) is closed on h-VOR adaptation (i.e., the network closed via NO making up a negative feedback loop). We considered four different NO configurations: (a) reversed NO connectivity (ipsi-lateral connections), (b) reversed NO connectivity with cross-connected micro-zones (contra-lateral connections), (c) direct NO connectivity (ipsi-lateral connections), and (d) direct NO connectivity with cross-connected micro-zones (contra-lateral connections). Please see the upper panel schematic diagram of Fig. 4 to visualise the connection patterns and the micro-complex cross-connections of these four NO configurations.

To provide a fair performance comparison amongst these NO configurations all the cerebellar neural elements remained equal except for the NO connectivity patterns. Hence, impaired h–VOR adaptation performances (Fig. 4B, and Fig. S6) could only be caused by an inadequate EC modulation. This modulation,

in turn, partially impaired the CF driven plasticity, where the consequences were reflected in the synaptic weight distributions at the PF–PC & MF–MVN synapses (Fig. S7). We found the reversed NO connectivity was better suited for VOR adaptation (Fig. 4A & C, Fig. S6), i.e., Pearson correlation coefficient obtained PCC_a = 0.999 ± 0.0001 vs. PCC_b = 0.9890 ± 0.0001, PCC_c = 0.954 ± 0.010, PCC_d = 0.849 ± 0.017 (mean ± std). Cross connecting the agonist and antagonist micro-zones whilst maintaining a reversed structural NO connectivity led to satisfactory results due to the symmetric nature of the h-VOR adaptation task (Fig. S7). The agonist/antagonist action was reversed although the overall NO inhibitory activity generated remained similar to the optimum configuration (Fig. S7) as did the subsequent electrical coupling modulation. The sensed error per micro-zone, although similar due to the VOR task symmetry, was not reversed thus originating a certain temporal misalignment between the IO maximum actions and the corresponding MVN counteractions. This misalignment caused a lack of precision during h-VOR adaptation that was reflected in the eye velocity curve, i.e., the sinusoidal peak was decreased and replaced by a sub-optimal centred plateau (Fig. 4B, and Fig. S6)

The last two configurations show that the reversed NO connectivity was the main contributor to the best electrical coupling modulation (Fig. S7) since it allowed for a gradual inhibitory action from C5 towards C1. C5 activity was modulated by the most active MVN whereas C1 was modulated by the least active MVN according to the IO–PC–MVN connectome (see Methods). Significantly, the reversed NO connectivity pattern was also crucial in maintaining the olivary "single-neuron dynamics" under GABAergic activations caused by MVN neural drives during the initial VOR stages, thus confirming Kawato's hypothesis (Fig. S8).

2.3. The NO delay in VOR adaptation

The long latency of the fibres at the NO inhibitory pathway is intriguing (Bengtsson & Hesslow, 2006). The peak inhibition in the inferior olivary cells experiences an incremental latency that varies with the size of the species. We tested the influence of incremental onset latency at the NO fibres during h-VOR adaptation. We considered three different NO delay configurations: (a) NO delay paired with the biological sensory–motor delay; this sensory–motor delay (100 ms) included the time period elapsed from the sensory information reception to information transmission along the nerve fibres, neural processing time responses and the final motor output response (Sargolzaei et al., 2016); (b) NO delay with half of the biological sensory–motor delay (50 ms); and (c) NO with no delay (Fig. 5 upper panel). To provide a fair performance comparison amongst these three different NO delay configurations, all the cerebellar neural elements remained equal except for the NO delays. Hence, impaired h–VOR adaptation performances (Fig. 5B) could only be caused by an inadequate EC modulation that partially impaired CF driven plasticity, where the consequences were reflected in the synaptic weight distributions at PF–PC & MF–MVN synapses (Fig. S9). We found that increasing levels of NO delay towards matching the biological sensory–motor delay (100 ms) made the h-VOR adaptation improve progressively (Fig. 5A & C), i.e., the Pearson correlation coefficient obtained PCC_a = 0.9984 ± 0.0003 vs. PCC_b = 0.9960 ± 0.0005 vs. PCC_c = 0.9920 ± 0.0008 (mean ± std), and we obtained an almost optimum shape of the counteractive eye-velocity curve (Fig. 5B).

The STDP mechanism (Luque et al., 2016) at PF–PC synapses accounted for the sensory–motor pathway delay (see Methods) by maximising the effect of the presynaptic spikes arriving through the PFs during the 100 ms time window before the postsynaptic CF spike arrival (Kawato & Gomi, 1992; Luque et al.,
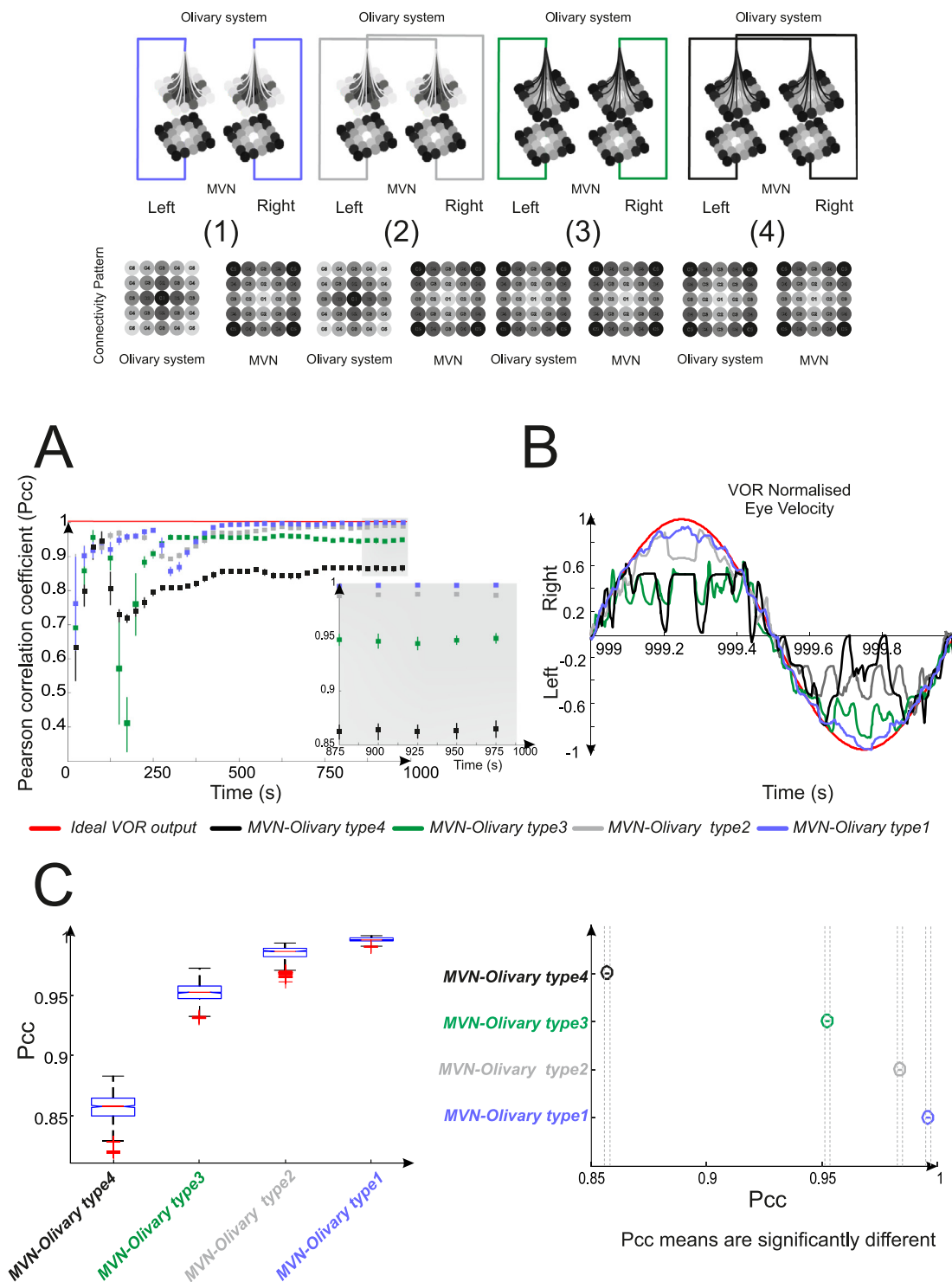
Fig. 4. Nucleo-olivary pattern connectivity. The cerebellar model embedding two micro-complexes. The upper panel (diagram) depicts the four connectivity patterns through which the IO–PC–MVN sub-circuitry is closed via the NO pathway during h–VOR adaptation (1 Hz h–VOR during 1000 s). (1) Reversed NO connectivity, i.e., MVN at C1 to IOs at C5, MVN C2–IOs C4, MVN C3–IOs C3. (2) Reversed NO connectivity, i.e., MVN at C1 to IOs at C5, MVN C2–IOs C4, MVN C3–IOs C3 with cross-connected micro-zones. (3) Direct NO connectivity, i.e., MVN at C1 to IOs at C1, MVN C2–IOs C2, MVN C3–IOs C3 MVN C4–IOs C4, MVN C5–IOs C5. (4) Direct NO connectivity, i.e., MVN at C1 to IOs at C1, MVN C2–IOs C2, MVN C3–IOs C3 MVN C4–IOs C4, MVN C5–IOs C5 with cross-connected micro-zones. **(A)** Pearson's coefficient evolution curves during h-VOR adaptation suggests the reversed NO connectivity to be the most adequate in regulating electrical coupling during cerebellar adaptation. Mean and standard deviation of the Pearson's coefficient curves are plotted (each 25 s) during h-VOR adaptation (1 Hz, h–VOR during 1000 s, VOR gain & phase in Fig. S6). **(B)** Eye velocity obtained for the four connectivity patterns after VOR adaptation (1 Hz, h-VOR during 1000 s, synaptic distributions for the four connectivity patterns at PF–PC and MF–MVN synapses in Fig. S7). **(C)** Figure C left, performance comparison (Pearson coefficient values) across the 4 NO connectivity patterns during h–VOR adaptation (over last 500 s after learning reaches a stable state). Figure C right depicts a multiple comparison post hoc test across the 4 Pearson's coefficient evolution curves obtained during h–VOR adaptation (over last 500 s after learning reaches a stable state). Statistically significant differences were found amongst these curves (ANOVA $F_{(3,2100)} = 3 \times 10^4$, $p < 10^{-50}$) indicating the reversed NO connectivity the best performing pattern. Reversed NO connectivity also helped maintain olivary "single dynamics" at early h–VOR adaptation stages (See Fig. S8). (For interpretation of the references to colour in this figure legend, the reader is referred to the web version of this article.)
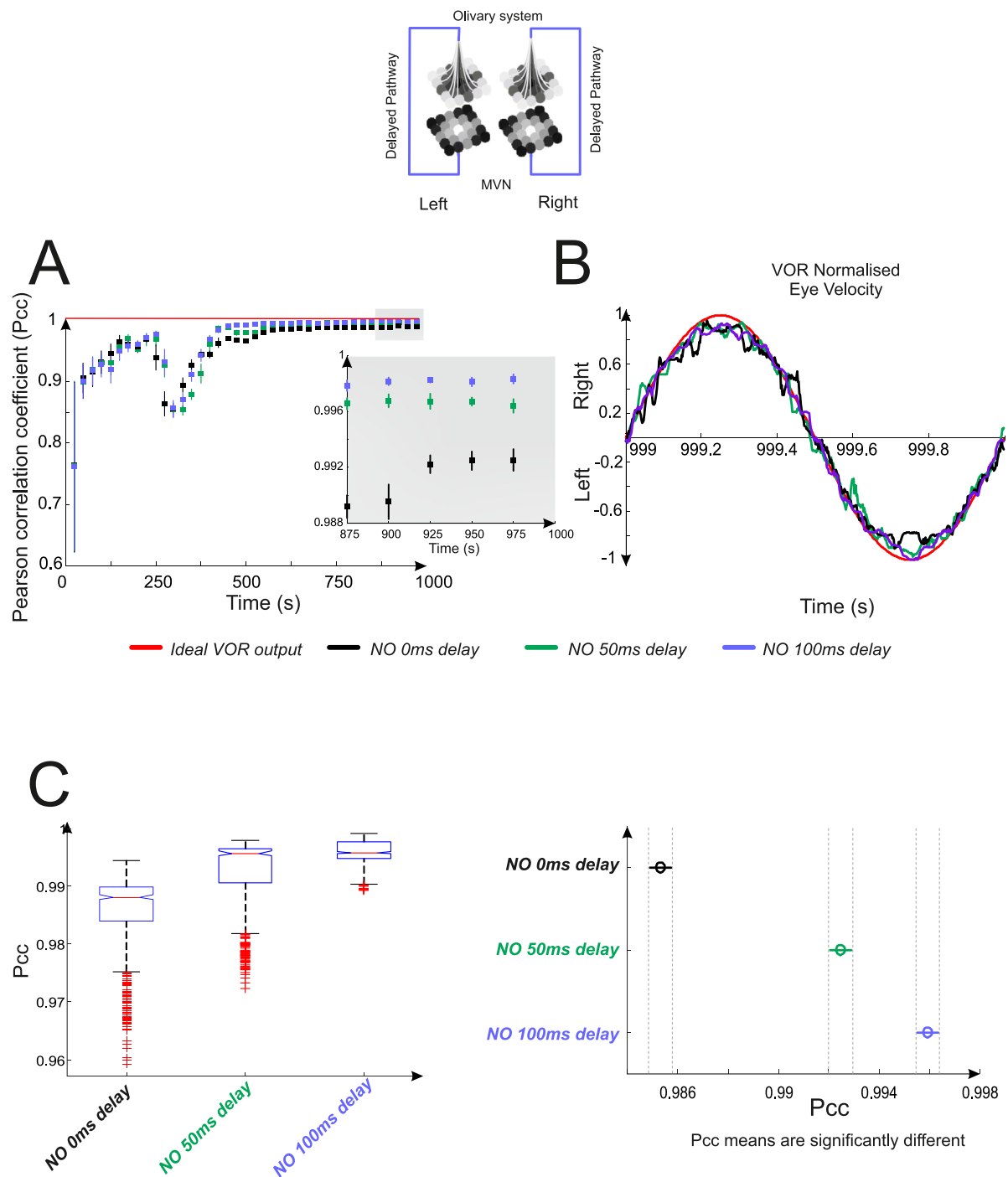
Fig. 5. Latency in nucleo-olivary afferents. **(A)** Pearson's coefficient evolution curves for testing the influence of an incremental onset latency at the NO fibres (Bengtsson & Hesslow, 2006) during h-VOR adaptation (1 Hz, h-VOR during 1000 s). Three different NO delay configurations: (a) NO delay paired with the biological sensory–motor delay (100 ms delay, purple curve). (b) NO delay half of the biological sensory–motor delay (50 ms delay, grey curve) (c) NO with no delay (0 ms delay, black curve). Mean and standard deviation of the Pearson's coefficient curves are plotted (each 25 s) during h-VOR adaptation (1 Hz, h-VOR during 1000 s). A latency aligned with the sensory–motor delay slightly favours h-VOR adaptation in terms of precision. **(B)** Eye velocity obtained for three delay configurations after VOR adaptation (1 Hz h-VOR during 1000 s, synaptic distributions for the three delay configurations at PF–PC and MF–MVN synapses in Fig. S9). **(C)** Figure C left, performance comparison (Pearson coefficient values) across the 3 NO delay configurations during h–VOR adaptation (over last 500 s after learning reaches a stable state). Figure C right depicts a multiple comparison post hoc test across the 3 Pearson's coefficient evolution curves obtained during h–VOR adaptation (over the last 500 s after learning reaches a stable state). Statistically significant differences were found amongst these curves (ANOVA $F_{(2,1575)} = 462$, $p < 10^{-50}$) indicating the NO delay paired with the biological sensory–motor delay, the best performing configuration. (For interpretation of the references to colour in this figure legend, the reader is referred to the web version of this article.)

2011a, 2011b, 2019). A NO delay matching the STDP 100 ms time window implied a temporal cause–effect alignment between the adaptive action undergone by the PCs together with their MVN

consequences, and the NO modulation of the EC at the olivary system, which was driving the sensed error into the cerebellar model. Our model predicted the need for NO delays in the

same order of magnitude as the biological sensory–motor delay to attune the tri-synaptic negative-feedback loop conformed by IO–PC–MVN–IO.

2.4. The IO axon collaterals to MVN provide for a forward loop in VOR adaptation

The IO cells synapse PCs via CFs in the cerebellar cortex and they project collateral axons to the MVN. However, the implications of this excitatory pathway remain to be elucidated (Baumel et al., 2009; Uusisaari & De Schutter, 2011). This connection has been proposed as a biological mechanism providing speed-up and stabilisation of cerebellar learning (Luque et al., 2014). It was conceptually demonstrated that the coexistence of the IO–MVN connection with different forms of supervised plasticity based on local activity levels (at PF–PC and MF–MVN) provided speed-up adaptation convergence whilst prevented instability as a result of over-excitation or saturation (Luque et al., 2014; Turrigiano & Nelson, 2004). In these studies this hypothesis was tested in a control scheme for the action of the IO axon collaterals to slowly decrease their contribution to cerebellar adaptation as the learning proceeds, yet neither the STDP mechanisms, nor the neural network, or the spiking neurons were present. Merely a cerebellar model based on firing rate (analogue signals) was used (Luque et al., 2014). In our study, we have tested and validated the learning speed-up and stabilisation capabilities of the IO collaterals to MVN during h-VOR adaptation by testing the cerebellar adaptation capability in the presence or absence of IO–MVN blockades. This can be done experimentally by infusing AMPA receptor antagonist NBQX and the NMDA receptor antagonist APV (Longley & Yeo, 2014). We verified that the IO–MVN excitatory action was needed and, indeed, indispensable to drive the MVN into their quasi-steady firing rate regimes (∼200 Hz) at early learning stages (450 s vs. 750 s, see Fig. 6A) favouring MVN activations upon learning initialisation (Fig. 6A, zoom in). The Pearson correlation coefficient also predicted a 60% faster convergence of h-VOR adaptation (Fig. 6B) and better accuracy (i.e., Pcc = 0.99 ± 0.001 vs. Pcc = 0.95 ± 0.0135, mean ± std) in the absence of IO–MVN blockades.

We also evaluated the stabilisation capability supported by the IO collaterals. The MVN neural activity histograms (Fig. 7, left panels) over the first 100 s of h-VOR simulation demonstrated that in all cases (MVN connected to IO located at C1, C2, C3, C4, and C5) the IO collaterals to MVN helped anticipate the cerebellar output. The cross correlation between the histograms obtained in the presence/absence of IO–MVN blockades (Fig. 7 left zoom in) indicated earlier and more effective MVN actions; i.e., Lag $_{MVN\_C1}$ = 0.204 s, Lag $_{MVN\_C2}$ = 0.203 s, Lag $_{MVN\_C3}$ = 0.190 s, Lag $_{MVN\_C4}$ = 0.188 s, Lag $_{MVN\_C5}$ = 0.187 s with differences in mean frequency of Freq $_{MVN\_C1}$ = 3.0x, Freq $_{MVN\_C2}$ = 3.75x, Freq $_{MVN\_C3}$ = 3.80x, Freq $_{MVN\_C4}$ = 3.5x, Freq $_{MVN\_C5}$ = 3.5x.

The MVN neural activity histograms (Fig. 7, right panels) over the last 100 s of h-VOR simulation demonstrated that in all cases (MVN connected to IO located at C1, C2, C3, C4, and C5) the IO collaterals to MVN helped to better adjust the final cerebellar output. The cross correlation between the histogram envelopes obtained in the presence or absence of IO–MVN blockades (Fig. 7, right zoom in) indicated a reduction of lag between MVN actions after learning; i.e., Lag $_{MVN\_C1}$ = −0.058 s, Lag $_{MVN\_C2}$ = −0.076 s, Lag $_{MVN\_C3}$ = −0.025 s, Lag $_{MVN\_C4}$ = −0.026 s, Lag $_{MVN\_C5}$ = −0.045 s with negligible differences in mean frequency Freq $_{MVN\_C1}$ = 1.0x, Freq $_{MVN\_C2}$ = 1.1x, Freq $_{MVN\_C3}$ = 1.20x, Freq $_{MVN\_C4}$ = 0.75x, Freq $_{MVN\_C5}$ = 0.6x. The MVN action in the presence of IO collateral blockades moved slightly ahead indicating a higher dispersion of most action potentials during the h-VOR adaptation process. IO collaterals contributed to strengthening the focus of most action potentials on a narrower timing window ∼[0.3 s–0.6 s] (with IO collaterals contribution) vs. [0.2 s–0.8 s] (without).

3. Discussion

The MVN constitutes the final output stage of the h-VOR cerebellar adaptation system. This final stage takes effect upon the rest of the VOR cerebellar circuitry via the efferent projections of MVN. Despite the plethora of cerebellar theories proposed, the functionality of the NO pathway, directly linking cerebellar output with input, has systematically been overlooked, hampering an effective comprehension of cerebellar adaptation. In this study, we have aimed to elucidate how and to what extent the GABAergic synaptic inputs from the NO pathway are relevant to cerebellar adaptation.

We first addressed the uncovered question of how GABAergic synaptic input may short-circuit the current flow between electrically coupled IO neurons. We modelled a minimalistic olivary system in lattice configuration (5 × 5 IO network) in which each IO cell was equipped with "dendritic current" flowing into other cells through electrical coupling. We then quantified the modulation of the electrical coupling amongst IO neurons by the NO inhibitory inputs whilst a steady-state nucleo-olivary response was evoked using inhibitory currents injected to the olivary system. We mimicked the in-vivo set-up proposed by Lefler et al. (2014) in which NO neurons were transfected with channelrhodopsin to specifically activate/deactivate this afferent pathway. We verified that activations of this NO pathway reduced the coupling coefficient (CC) and predicted its linear reduction with the coupling distance to the neuron into which the negative step current was injected. More significantly, a positive step current predicted an exponential reduction of the CC with the coupling distance to the injected neuron. Cerebellar h-VOR adaptation deploys under these positive current-injecting conditions and therefore the outcoming exponential decrease of CC must play a role in the olivary timing function. We found inter-spike distance (ISI) increments reflected in exponential decrements of the IO spike frequencies with the coupling distance, suggesting a Gaussian-like distribution for the spike generation that was centred in the injected neuron.

The results of our model are in concordance with the *adaptive coupling hypothesis* formulated by Kawato's modelling studies (Kawato et al., 2011; Tokuda et al., 2017, 2013) only if we consider a CC regulation by the GABAergic NO path. In the absence of GABAergic NO activations and positive current-injecting conditions, our model showed that a strong coupling induced highly synchronised activities for IO neurons able to generate initial rapid responses to sensory inputs still to be learnt. On the other hand, a progressive coupling reduction as the contribution of GABAergic NO activations became more prevalent led to the decrease of the synchronised activities of the IO neurons. The transition from a homogeneous to a Gaussian distribution for the olivary spike generation owing to a CC regulation must provide a sort of spiking adaptive mechanism deployed during cerebellar motor adaptation. This adaptive mechanism was then studied considering a wider perspective; the triangle closed-loop circuit consisting of PC, IO, and MVN embedded in a cerebellar-dependent adaptation task, the h-VOR (Fig. 1A).

Cerebellar learning, and particularly PC and MVN response adaptation, is necessary to mediate online changes in VOR gain control (De Zeeuw et al., 1998; Rambold et al., 2002). The cerebellar model presented here mimicked the main properties of the cerebellar microcircuit. It incorporated the olivary system previously described and embodied spike-based LTP/LTD plasticity mechanisms at two synaptic sites; PF–PC and MF–MVN synapses (Fig. 1B). The model captured the fact that CF discharges encoded the retinal slips that drove VOR adaptation, as seen in experimental studies (Stone & Lisberger, 1990). During VOR adaptation, LTD predominantly blocked LTP at PF–PC synapses.
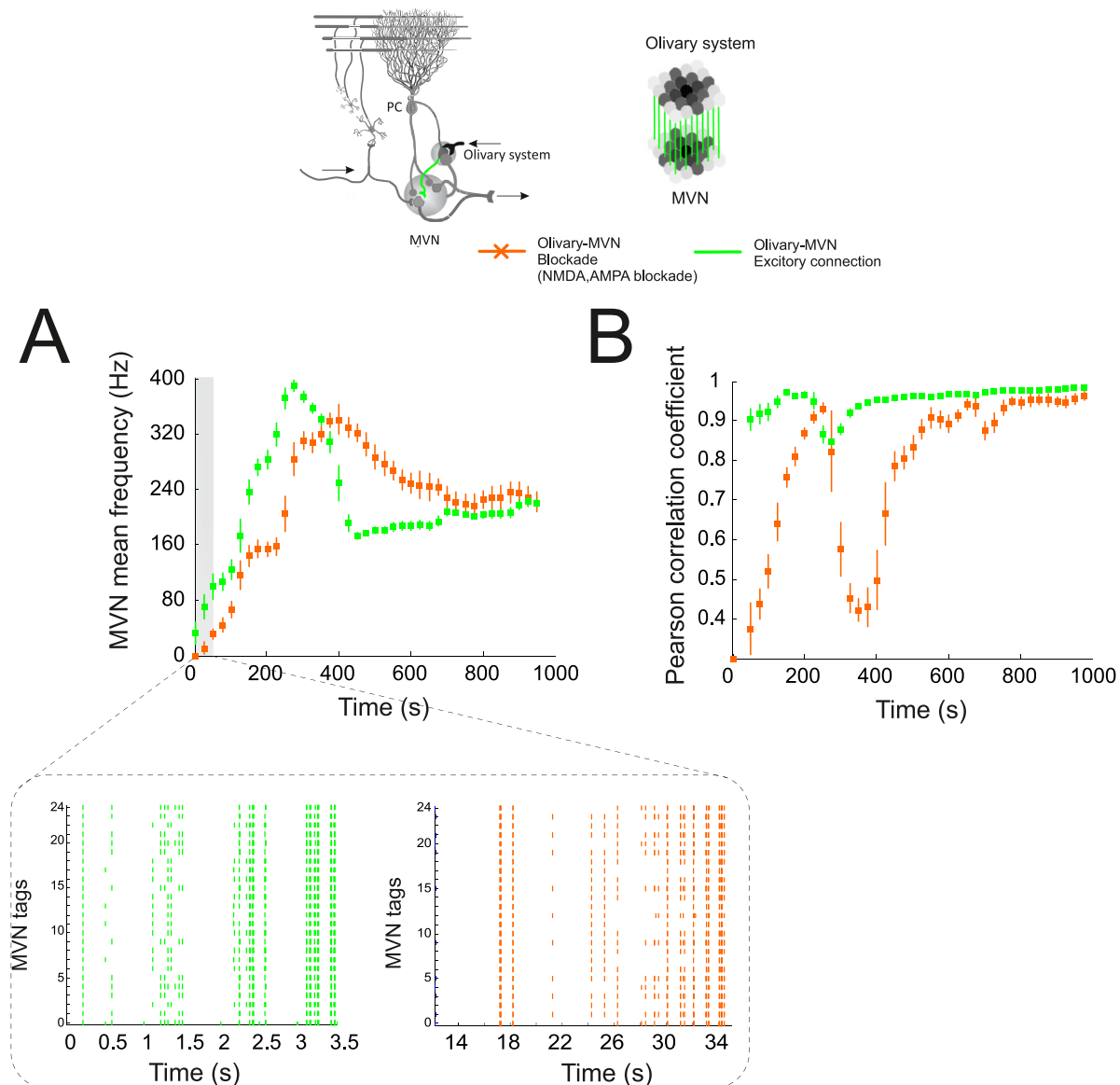
Fig. 6. The IO axon collaterals to MVN provide for speed-up and stabilisation of cerebellar learning. The diagram depicts a schematic representation of the IO axon collaterals to MVN connections recorded during h-VOR adaptation (1 Hz, h-VOR during 1000 s). AMPA and NMDA blockades were simulated as if AMPA and NMDA antagonists were infused. **(A)** MVN mean frequency indicates that the IO–MVN excitatory action drives the MVN faster into their quasi-steady firing rate regimes thus favouring MVN activations upon learning initialisation. **(B)** The evolution of the Pearson correlation coefficient in the presence or absence of AMPA and NMDA blockades verifies that the IO–MVN connection is central in accelerating convergence during h-VOR adaptation. (For interpretation of the references to colour in this figure legend, the reader is referred to the web version of this article.)

This resulted in a synaptic efficacy decrease as a CF spike reached the target PC (error-related signal). In particular, a CF spike is more likely to depress a PF–PC synapse if the PF was active 50–150 ms prior to the CF spike arrival (Kettner et al., 1997; Luque et al., 2016; Raymond & Lisberger, 1998). LTP at our modelled PF–PC synapses was non-supervised and it strengthened a connection upon each PF spike arrival at the target Purkinje cell. This plasticity mechanism did not need to modulate the input provided by CFs to counter LTD and decrease the VOR gain, in accordance with in-vitro experiments (Belmeguenai et al., 2008; Carey & Regehr, 2009; He et al., 2013). CF-evoked PC spikes, in turn, similarly shaped the MF–MVN synapses (Luque et al., 2016). A PF spike reaching the target MVN resulted in a synaptic efficacy decrease at the MF–MVN synapses. LTP at our modelled MF–MVN synapses was also non-supervised and it strengthened a connection upon each MF spike arrival at the target MVN.

Early cerebellar learning stages entail large sensed retinal slips that generated a large number of CF complex spikes. Large CF complex spike numbers, in turn, elicited large MVN activations via CF–MVN collaterals and high LTD levels at PF–PC cell synapses causing a reduction of the inhibitory action of PC onto MVN. This inhibitory action was further enhanced by the synaptic plasticity mechanism at MF–MVN synapses driven by the CF-evoked PC spikes. Consequently, the GABAergic NO activity increased concomitantly with the MVN neural activity causing IO EC to be diminished and preventing the "single neuron" CF complex spike dynamics hypothesised, i.e., complex spike homogeneous distribution at the early cerebellar learning stages (Kawato et al., 2011; Tokuda et al., 2017, 2013). We found the topology of GABAergic NO pathway to be key in facilitating the transitions from a homogeneous to a Gaussian complex spike distribution and vice versa, thus conciliating the *adaptive coupling hypothesis* and the h-VOR STDP mechanisms beneath. Blocking the GABAergic NO pathway, which can be done experimentally by using a small amount of GABA-blocker bicuculline (Bengtsson & Hesslow,
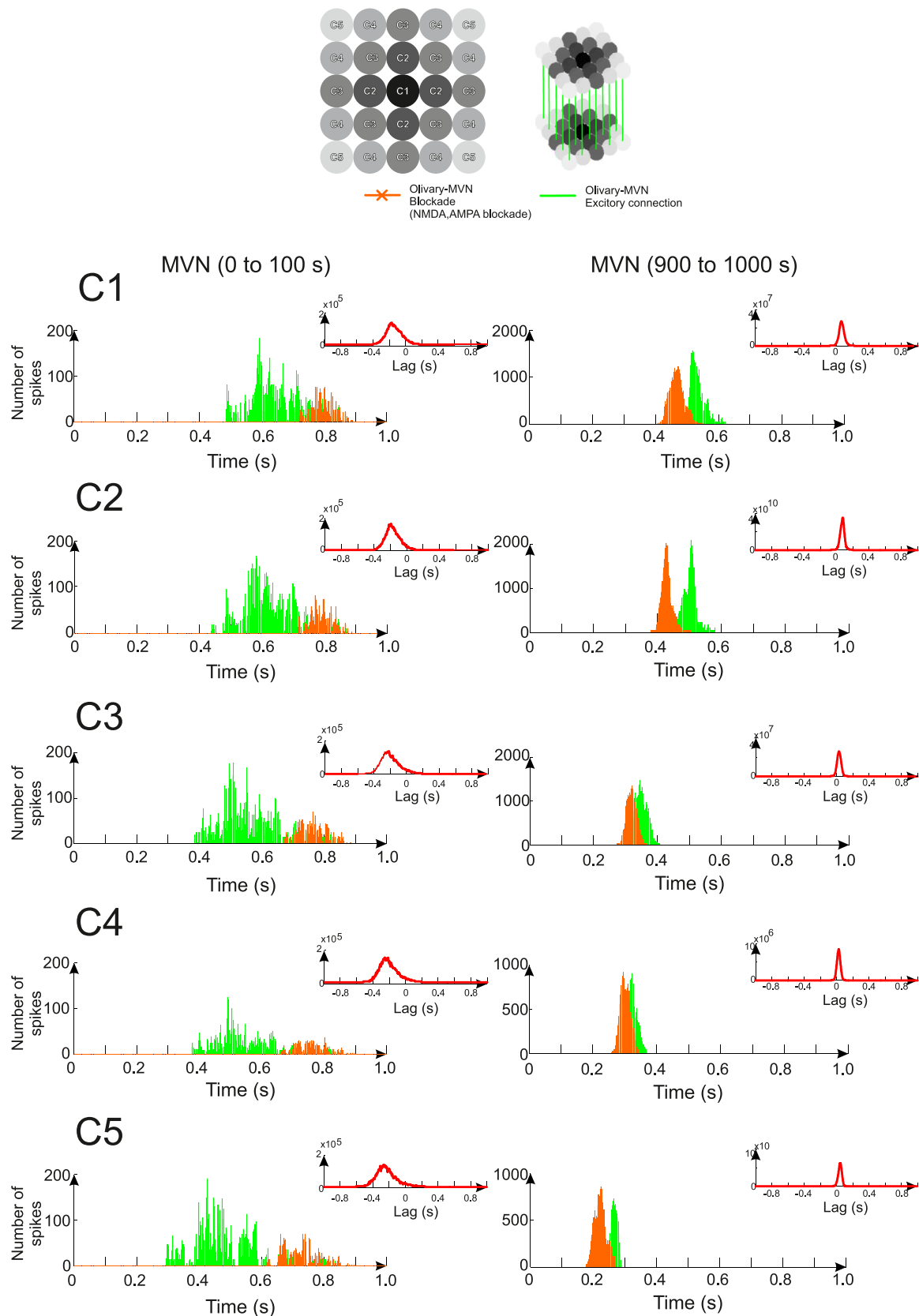
Fig. 7. IO collaterals to MVN improve the temporal adjustment of the cerebellar output. The diagram depicts the schematic representation of the IO axon collaterals to MVN connections recorded during h-VOR adaptation from a 5 × 5 squared section of the olivary system in lattice configuration. Two histogram columns depicting the action potentials driven by IO axon collaterals to MVN (from a 5 × 5-squared IO section activity) in the presence or absence of AMPA and NMDA blockades before (left column) and after learning (right column) of the h-VOR adaptation process. Zoom-in depicts the lag between the histogram envelopes. The MVN action potentials under AMPA and NMDA blockades are dispersed across the temporal 1 Hz/1 s head rotation during the h-VOR adaptation process. IO collaterals helped to confine most action potentials on a narrower time window gaining temporal precision. (For interpretation of the references to colour in this figure legend, the reader is referred to the web version of this article.)

2006), would prevent the transition from a homogeneous to a Gaussian distribution on the complex spike generation. Our results predict a loss in granularity and specificity of MF–MVN synaptic weights as result of a high degree of synchronisation in complex spike modulation throughout the olivary system, which ultimately compromises accuracy and learning consolidation during h-VOR adaptation.

The topology of the modelled GABAergic NO pathway followed experimentally reported olivo-cortical projections (De Zeeuw et al., 1997). Hence, NO afferents project specifically to olivary neurons in, or at least close to, the same micro-complex (Bengtsson & Hesslow, 2006) which would prevent NO inhibitory effects amongst micro-complexes. Note that a functional module of the cerebellum comprises a functional unit of the cerebellar cortex (micro-zone), a parasagittal strip of PC cells with a common CF input, and the group of neurons in the olivary system and MVN to which the micro-zone is connected (Ito, 2001). We speculated about the anatomical nature of the NO inputs assuming the PC control is always via MVN. We disrupted the integrity of the OCNO loop (Uusisaari & De Schutter, 2011) within the same micro-zone. We crossed NO pathways between micro-complexes to mimic NO afferents driven by collaterals of other nuclear cells consistent with the hypothesis of Bengtsson and Hesslow (2006). The symmetry of h-VOR adaptation (clockwise and anti-clockwise symmetrical correction) allowed a crossed NO pathway for a sufficient performance in relation to the direct NO pathway, thus confirming the possible stimulation of two different NO paths for a common inhibitory mechanism with almost indistinguishable effects as was experimentally found in Bengtsson and Hesslow (2006) and Svensson et al. (2006). Strikingly, the intrinsic connectivity pattern of the NO afferent projections to olivary neurons within the same micro-complex revealed itself as being instrumental for h-VOR adaptation. Our results envisage the reversed connectivity NO pattern (see Fig. 5 upper panel) to be pivotal in helping to desynchronise IO activations within the same micro-complex during h-VOR adaptation, i.e., reversing the IO–PC–MVN connectivity via MVN–IO connections improved the performance of h-VOR adaptation. Moreover, the NO reversed connectivity also proved to be crucial in facilitating the olivary "single neuron dynamics" at initial learning stages as hypothesised in Kawato et al. (2011), even in the presence of GABAergic NO activations via MVN.

The picture that emerges from speculating about NO path topology gets more interesting when considering the long latency of the inhibition under direct stimulation of NO fibres. Actually, the long latency peak inhibition seems to increase with the size of species, i.e., about 30 ms in ferrets, up to 50 ms in cats (Hesslow, 1986; Svensson et al., 2006). Neither the thinness of the NO fibres nor a di- or tri- synaptic NO pathway explains this long latency but more probably a slow GABA receptor mechanism. This NO long latency combined with low conduction velocities of CFs is perceived as a nuisance in explaining the fast adjustments of movements associated to the cerebellum functionality rather than a necessary condition for the cerebellar system adaptation. Our model predicts this latency as a functional feature providing the necessary timing correspondence between NO latency and sensory–motor pathway delay. A NO latency within the 50–100 ms time-range in which CF spikes were more likely to depress a PF–PC synapse was found to better align the olivary teaching action and its consequence accordingly during h-VOR adaptation.

We finally found the EC modulation role of the NO pathway being complemented during h-VOR adaptation by its olivary–nuclei pathway counterpart. CFs directly innervate the vestibular nuclei from the IO and provide a strong neural drive related to the state of the olivary network, i.e., graded information within the

CF bursts, to the MVN cerebellar nuclei (Najac & Raman, 2017). We found that CF collaterals, as experimentally hypothesised in Najac and Raman (2017) and Pickford and Apps (2017), may serve different functional roles, i.e., CF collaterals in juvenile mice shape the cerebellar functional micro-circuit, whereas in adult mice they provide IO neural state information (Pickford & Apps, 2017). At initial h-VOR learning stages, the IO collateral activation evoked prompt MVN synaptic responses that drove them into their optimum frequency regime required for the long-term plasticity to fully develop. "Single-neuron" dynamics in the olivary network were translated into a coarse but also fast neural drive (Luque et al., 2014). Conversely, at final h-VOR learning stages, the IO collateral activation was signalling "multiple-neuron" dynamics, i.e., graded information within the CF bursts, which allowed the MVN to narrow down their active timing windows to better shape the VOR adaptation oculo-motor commands.

4. Materials & methods

4.1. Calculating the coupling coefficient (CC)

The electrical coupling strength was estimated using steady-state CC (Hoge et al., 2011). CC were calculated by injecting a current pulse into the central IO cell, C1, either negative (Supplementary, Fig. S1) −30 pA, or positive (Fig. S2) from 30 to 40 pA (IO current range activation) for 1 s. Concurrently, we measured the resulting membrane potential in all the IO cells within the lattice located from C2 to C5 (see Supplementary Fig. S1 & Fig. S2). Note that the CC between C1 and C2 IO cells, CC_{1-2}, would be calculated as V2/V1 ratio where V1 is the membrane potential in the central-injected IO and V2 is the corresponding membrane potentials in the non-injected IO cells at C2. The CC is given in Eq. (1):

$$CC_{\Delta vc\_k} = \frac{\Delta V_{ck}}{\Delta V_{c1}} \tag{1}$$

whereas the coupling coefficient reduction Δ_{cc} is defined as the difference between CC Eq. (2):

$$\Delta_{cc\_k} = CC_{\Delta vc\_k} - CC_{\Delta vc\_(k+1)} \tag{2}$$

where ΔV_{c1} defines the membrane potential difference between the resting and the depolarisation phase voltage at the central-injected IO. ΔV_{ck} defines the membrane potential differences found in the kth IO neurons that are concentrically located in the olivary lattice arrangement from C2 to C5. Note that the IO membrane potential prior entering its depolarisation phase is configured at 50 mV (see Fig. S2A, zoom-in). To better understand the potential dynamics of the olivary network membrane see Supplementary and Figure S2 in Luque et al. (2022).

4.2. Spike train analysis

The synchronisation of neuronal firings at MVN (connected to the olivary system disposed in lattice configuration Nobukawa & Nishimura, 2016) was quantified using the coherence measure (CM) based on the normalised cross-correlations of neuronal spike train pairs obtained in MVN at C1, C2, C3, C4 and C5 (Wang & Buzsáki, 1996) under *GABAergic* NO de/activations (see the neural network model). The coherence between two MVN neurons (n_1 and n_2) was measured by their cross-correlation of spike trains at zero time lag within a time bin of $\Delta t = \tau = 0.002$ s. Each h-VOR trial (T = 1 s) was split into small bins of τ with the MVN neurons spike trains given in Eq. (3):

$n_1(i) = 0 \, or \, 1$

$i = 1, 2, 3 \ldots, N \quad where \left(\dfrac{T}{N} = \tau \right) \tag{3}$

$n_2(i) = 0 \, or \, 1$

where N is the number of spikes and the coherence measure is given by Eq. (4):

$$CM_{n_1 n_2}(\tau) = \frac{\sum_{i=1}^{N} n_1(i) \cdot n_2(i)}{\sqrt{\sum_{i=1}^{N} n_1(i) \cdot \sum_{i=1}^{N} n_2(i)}} \qquad (4)$$

4.3. Synaptic weight analysis

The synaptic weight evolution at MF–MVN synapses was measured using the Discrete Wavelet Transform (DWT) (Latorre et al., 2013). The synaptic weight values of certain synapses were considered as an image and the synaptic weight evolution as a sequence of images. These images and sequences of images were analysed using wavelet based techniques (Stollnitz et al., 1996). The DWT provided a number of coefficients that characterised the whole complexity of the images (Latorre et al., 2013). A small number of wavelet coefficients define an image that only holds a few low-resolution components, i.e., high compression rate achieved for a low complexity image. Conversely, a large number of coefficients define a complex image and high resolution (details), i.e., a low compression rate cannot be achieved for a highly complex image. We considered the spatial–temporal patterns generated by the MF–MVN synaptic weight values as sequences of images for which we estimated their compression rate by calculating the number of DWT coefficients. The spatio-temporal pattern of the MF–MVN synaptic weights is translated into a one-dimensional signal that represents the evolution of the spatio-temporal pattern complexity during VOR adaptation (Luque et al., 2022).

4.4. VOR analysis and measuring

As in Luque et al. (2019, 2022), we simulated h-VOR experiments with subjects experiencing sinusoidal (∼1 Hz) whole body rotations in the dark (Van Alphen et al., 2001). The sinusoidal-like curves accounting for eye and head velocities (Fig. 1A) were analysed by using the discrete time Fourier transform (FT). The VOR gain (G), Eq. (5), was calculated as the ratio between the first harmonic amplitudes (HA$_1$) of the forward Fourier eye- and head-velocity transforms:

$$G = \frac{HA_1^{eye-velocity}}{HA_1^{head-velocity}} \qquad (5)$$

Conversely, the cross-correlation *(xcorr)* of the eye (e) and head (h) velocity sinusoidal-like curves was used to assess the VOR shift phase (P), (Eq. (6)):

$$P = xcorr = (e * h)[\gamma] \overset{def}{=} \sum_{n=-\infty}^{+\infty} e^*(n)\, h(n+\gamma) \qquad (6)$$

where e* defines the complex conjugate of e, and γ the lag, i.e., shift phase. The ideal shift phase value between eye and head velocity is ±0.5 after normalisation, being the cross-correlation values ranging within $[-1, 1]$, which corresponds to a shift phase interval of $[-360°, 360°]$.

The cross-correlation may also be used to measure the degree of similarity between two time series i.e., the eye (e) and head (h) velocity time series (Eq. (6)). However, this measure provides for different cross-correlation values for two identical time series with different energy. The Pearson correlation coefficient solves the problem (Eq. (7)).

$$Pearson's\ r = \frac{\sum_{i=1}^{n} (e_i - \bar{e}) \cdot (h_i - \bar{h})}{\sqrt{\sum_{i=1}^{n} (e_i - \bar{e})^2} \cdot \sqrt{\sum_{i=1}^{n} (h_i - \bar{h})^2}} \qquad (7)$$

where n denotes the number of time series samples. e_i and h_i are the individual sample points whereas $\bar{e}$ and $\bar{h}$ stand for the sample mean. *Pearson's r* absolute values range within $|0, 1|$ interval, where 1 denotes a linear correlation (positive or negative) between times series (similar time series) whereas zero indicates otherwise.

The Pearson's correlation coefficient was finally used as a complementary measure able to combine VOR gain and shift phase measurements as if they were unified in a single value.

4.5. Cerebellar spiking - neural network

Note that the methods within this subsection have been previously detailed in Luque et al. (2019). For the sake of clarity, here we provide an overview of the implemented cerebellar network and its connectome.

The cerebellar network model was at the core of a feed-forward control loop to compensate head movements via contralateral eye movements (Fig. 1A) (Luque et al., 2019, 2022). The implemented network consisted of five neural populations, namely: mossy fibres (MFs), granule cells (GrCs), inferior olive (IO) cells, Purkinje cells (PCs), and medial vestibular nuclei (MVN) (Eccles et al., 1967; Ito, 1984; Luque et al., 2019, 2022; Medina & Mauk, 1999, 2000; Voogd & Glickstein, 1998). The sensory–motor activity generated by 1-Hz simulated head rotations was transformed into MF neural patterns that encoded head velocity. MFs propagated this information to both MVN and GrCs. GrCs generated a sparse representation of head velocity signals and transmitted them to the PCs via the PFs. PCs also received the teaching signal from the CFs, i.e., IO axons, which encoded sensory-error information, i.e., retinal slips caused by the differences found between actual and target eye movements, (Stone & Lisberger, 1990). Finally, excitatory olivary CF collaterals along with inhibitory PC outputs contacted MVN neurons, which closed the loop through NO connections and generated the cerebellar output activity. MVN output targeted oculomotor neurons (OMNs), which drove eye movements. The CF–PC–MVN sub-circuit was divided in two symmetric micro-complexes that compensated for right and left head movements, respectively. STDP at two synaptic sites, i.e., PF–PC and MF–MVN (∼50 000 synapses, Fig. 1B), made the network adaptive by both LTP and LTD (Luque et al., 2016, 2019, 2022). The cerebellar model ran in EDLUT (Naveros et al., 2017, 2015; Ros et al., 2006), an open-source spiking neural simulator oriented to real-time computation and embodiment experimentation. Table 1 summarises the network connectivity parameters.

Mossy fibres (MFs). 100 MFs were modelled as input neurons that propagated the sensory–motor information into GrCs and MVN as in Luque et al. (2019).

Granular cells (GrCs). The granular layer was modelled using 2000 Leaky Integrate & Fire (LIF) cells as a state generator (Honda et al., 2011; Yamazaki & Tanaka, 2005, 2007, 2009) following a similar implementation than in Luque et al. (2019).

Purkinje cells (PCs). 200 PCs were modelled as Hodgkin–Huxley (HH) neuron models with one compartment and five ionic currents according to the PC model in Luque et al. (2019). Each PC received 2000 PF and 1 CF inputs. The PCs were aggregated into two populations of 100 neurons each; one population receiving inputs from 100 CFs encoding the rightwards eye-to-head movement difference and the second population receiving inputs from 100 CFs encoding the leftward difference. Each PC population, in turn, inhibited 100 MVN cells, accounting for either clockwise or counter-clockwise compensatory motor actions (ultimately driving the activity of agonist/antagonist ocular muscles).

Climbing fibres (CFs) and Inferior olive (IOs) cells. 200 IO cells were modelled as electrically coupled LIF neurons. The IO cells were aggregated into two populations of 100 neurons (see Table 1, lattice configuration Nobukawa & Nishimura, 2016) that coded clockwise and counter-clockwise retinal slips (sensed errors), respectively. CFs drove the teaching signal from the IO cells towards the PCs. Each CF contacted one PC and one MVN cell. Please refer to Luque et al. (2019) to understand the process of generating the external IO input activity related to the sensed retinal slips (error signal).

The IO cells were electrically interconnected via gap-junctions (GJ) and coupled following preferred directions that were not exactly aligned to the neural vicinity (Devor & Yarom, 2002) (i.e., the nearest IO cells are not always the cells that were coupled in the first place). These "preferred directions" were mimicked by using a 5 × 5 lattice topology as in Luque et al. (2022). The preferred paths are disposed radially from the centre of the grouped 5 × 5 IO cells to the corners (see the network connectivity parameters summarised in Table 1).

Medial vestibular nuclei (MVN). The MVN were modelled as 200 LIF cells and their neural activities generated the cerebellar model output. The MVN cells were aggregated into two populations of 100 neurons each that drive clockwise and counter–clockwise motor correction, respectively. Each MVN neuron received excitatory afferents from all the MFs, an inhibitory afferent from a PC and also an excitatory afferent from the CF which concomitantly innervates the same PC (i.e., the sub-circuit CF–PC–MVN was organised in a single micro-complex). The MVN closes the CF–PC–MVN loop via GABAergic projections onto the olivary network. The neural MVN activity was eventually converted into eye velocity (analogue signal) following Eqs. (8)–(10):

$$MVN_i(t) = \int_{t}^{t+T_{step}} \delta_{MVN_{spike}}(t) \cdot dt \tag{8}$$

$$MVN_{output}(t) = \alpha \cdot \left(\sum_{i=1}^{N=100} MVN_{clockwise_i} - \sum_{j=1}^{N=100} MVN_{anticlockwise_j} \right) \tag{9}$$

$$\alpha = \frac{h\_VOR \quad range(deg/s)}{N} \tag{10}$$

where α defines a constant that normalises the contribution of each MVN neuron activity output. i and j denote the MVN neuron tag from one to N, the total of MVN per sub-population (clockwise and anti-clockwise sub-population). $\delta_{MVN_{spike}}$ denotes the Dirac delta function representing the MVN spikes elicited and T_{step} (0.002 s) the temporal length of the sliding windows on which the MVN spiking activity is computed.

4.6. Neuron models

The LIF model (GrCs, MVN). These cell models were implemented according to Eqs. (11)–(17) as LIF cells with excitatory (AMPA and NMDA) and inhibitory (GABA) chemical synapses:

$$C_m \cdot \frac{dV}{dt} = I_{internal} + I_{external} \tag{11}$$

$$I_{internal} = -g_{rest} \cdot (V + E_{rest}) \tag{12}$$

$$I_{external} = -\left(g_{AMPA}(t) + g_{NMDA}(t) \cdot g_{NMDA_{inf}}\right) \cdot (V - E_{AMPA}) - \\ -g_{GABA}(t) \cdot (V - E_{GABA}) \tag{13}$$

where $I_{internal}$ stands for the internal currents and $I_{external}$ the external currents, V the membrane potential, and C_m the membrane capacitance. E_{rest} denotes the resting potential whereas E_{AMPA} and E_{GABA} denotes the reversal potential of each synaptic conductance,

and g_{rest} is the conductance causing the passive decay towards the resting potential. Conductances g_{AMPA}, g_{NMDA} and g_{GABA} integrate all the contributions provided from each receptor type (AMPA, NMDA and GABA) through individual synapses and follow decaying exponential function shapes (Gerstner & Kistler, 2002; Luque et al., 2019, 2022; Ros et al., 2006):

$$g_{AMPA}(t) = \begin{cases} 0, & t \le t_0 \\ g_{AMPA}(t_0) \cdot e^{-\frac{(t-t_0)}{\tau_{AMPA}}}, & t > t_0 \end{cases} \tag{14}$$

$$g_{NMDA}(t) = \begin{cases} 0, & t \le t_0 \\ g_{NMDA}(t_0) \cdot e^{-\frac{(t-t_0)}{\tau_{NMDA}}}, & t > t_0 \end{cases} \tag{15}$$

$$g_{GABA}(t) = \begin{cases} 0, & t \le t_0 \\ g_{GABA}(t_0) \cdot e^{-\frac{(t-t_0)}{\tau_{GABA}}}, & t > t_0 \end{cases} \tag{16}$$

Finally, g_{NMDA_INF} defines the NMDA activation channel.

$$g_{NMDA\_inf} = \frac{1}{1 + e^{62 \cdot V} \cdot \frac{1.2}{3.57}} \tag{17}$$

The LIF model incorporates electrical coupling (IO). This LIF model was implemented as a modification of the previous model in which the electrical synapse was added and NMDA suppressed as indicated in Eqs. (18), (19).

$$I_{external} = -g_{AMPA}(t) \cdot (V - E_{AMPA}) - g_{GABA}(t) \cdot (V - E_{GABA}) - I_{GJ} \tag{18}$$

$$I_{GJ} = \sum_{i=1}^{N} w_i \cdot (V - V_i) \cdot \left(0.6 \cdot e^{-\frac{(V - V_i)^2}{50^2}} + 0.4 \right) \tag{19}$$

where I_{GJ} stands for the current injected through the gap-junction (GJ) (Luque et al., 2022; Schweighofer et al., 1999), V is the target neuron membrane potential, V_i the i neuron membrane potential, w_i is the synaptic weight between the neuron i and the target neuron, and N is the total number of GJ current inputs. The parameters of the LIF cell used for each cell type (Granule, IO, and MVN cells) and synaptic receptor type can be found in Luque et al. (2022).

The HH mono-compartment model (PC). This was implemented using an HH with a single compartment including five ionic currents and two excitatory (AMPA) and inhibitory (GABA) chemical synapses as in Luque et al. (2019).

$$C_m \cdot \frac{dV}{dt} = I_{internal} + \frac{I_{external}}{Membrane \quad Area} \tag{20}$$

$$I_{external} = -g_{AMPA}(t) \cdot (V - E_{AMPA}) - g_{GABA}(t) \cdot (V - E_{GABA}) \tag{21}$$

$$I_{internal} = -g_k \cdot n^4 \cdot (V + 95) - g_{Na} \cdot m_0[V]^3 \cdot h \cdot (V - 50) - \\ -g_{Ca} \cdot c^2 \cdot (V - 125) - g_L \cdot (V + 70) - g_M \cdot M \cdot (V + 95) \tag{22}$$

where $I_{internal}$ defines the internal currents, $I_{external}$ the external currents, V the membrane potential and C_m the membrane capacitance. Conductances g_{AMPA} and g_{GABA} integrate all the contributions received by each chemical receptor type (AMPA and GABA) through individual synapses (Luque et al., 2019, 2022). These conductances followed a decaying exponential function shape (Eqs. (14), (16)).

In Eq. (22), g_M defines a muscarinic receptor suppressed potassium current, g_L a leak current, g_{Ca} a high-threshold non-inactivating calcium current, g_{Na} a transient inactivating sodium current, and g_K a delayed rectifier potassium current. Note that the dynamic evolution of each gating variable (n, h, c, and M) follows Eq. (23):

$$\dot{x} = \frac{x_0[V] - x}{\tau_x[V]} \tag{23}$$

Table 1
Summary of neurons and synapses.

Neurons			Synaptic weights (nS)		
Presynaptic neuron (number)	Postsynaptic neuron	Number of synapses	Type	Initial weight	Weight range
Mossy fibres (100)	Granular cells	8000	AMPA	0.35[a]	–
	Medial vestibular nuclei (200)	20 000	AMPA	0.0	[0, 10]
Inferior olive to inferior olive: 5 × 5 IO neuron squares connected radially from the centre to the corner of each 5 × 5 square (200). IO squares were partially overlapped (1 row & 1 column).		320	GJ	0.4	–
Climbing fibres (200)	Purkinje cells	200	AMPA	40	–
	Medial vestibular nuclei	200	AMPA	2.83	–
			NMDA	8.52	–
Granular cells (2000)	Purkinje cells	400 000	AMPA	3.4	[0,4]
Purkinje cell (200)	Medial vestibular nuclei	200	GABA	1.5	–
Medial vestibular nuclei (200)	Inferior olive	200	GABA	1.293	–

[a]Parameter used for generating the offline GrC activity. The GrC activity remained invariant during h-VOR adaptation. It was loaded in computation time to accelerate simulation time.

where x corresponds to variables n, h, c, and M. The equilibrium function is given by both the term $x_0[V]$ and the time constant $\tau_x[V]$. All the HH ionic conductance kinetic parameters and equilibrium functions can be found in Luque et al. (2019) .

4.7. Synaptic plasticity mechanisms

The adaptation of the cerebellar network model was driven by two STDP mechanisms at different synaptic sites. These STDP mechanisms balance LTP and LTD at PF–PC and MF–MVN synapses (see Luque et al., 2016 for an in-depth review of the implemented synaptic mechanisms).

PF–PC synaptic plasticity: The LTD/LTP balance at PF–PC synapses was based on Eq. (24):

$$LTD \Delta w_{PF_j-PC_i}(t) = \lambda_1 \cdot \int_{-\infty}^{IO_{spike}} k_1 \left(\frac{t - t_{IO_{spike}}}{\tau_{LTD}} \right) \cdot \delta_{PF_{spike}}(t)\, dt$$

$$\quad \text{if } PF_j \text{ is active at } t$$

$$LTP \Delta w_{PF_j-PC_i}(t) = \lambda_2 \cdot \delta_{PF_{spike}}(t) \quad const. \quad otherwise$$

$$(24)$$

where $\Delta W_{PF_j-PC_i}(t)$ stands for the weight change between the source jth PF and the target ith PC; $\tau_{LTD} = 100$ ms denotes the time constant that compensates for the sensory–motor delay; δ_{PF} refers to the Dirac delta function indicating the presence of an afferent spike from a PF (i.e., emitted by a GrC). $\lambda_1 = -0.0380$ nS defines the synaptic efficacy decrements; $\lambda_2 = 0.0230$ nS defines the synaptic efficacy increments; and finally the kernel function $k_1(x)$ (Luque et al., 2016, 2022) is defined as in Eq. (25):

$$k_1(x) = e^{-x} \cdot \sin(x)^{20} \tag{25}$$

The LTD convolution in Eq. (24) was computed on those presynaptic PF spikes that arrive 100 ms before a CF spike arrival, accounting for the sensory–motor pathway delay (Kawato & Gomi, 1992; Luque et al., 2011a, 2011b, 2014, 2022). Finally, as shown in Eq. (24), the amount of LTP at PF–PC synapses was fixed, with an increase in synaptic efficacy equal to λ_2 each time a spike arrived through a PF to the target PC.

MF–MVN synaptic plasticity: The LTD/LTP dynamics at MF–MVN synapses was based on Eq. (26):

$$LTD. \Delta w_{MF_j-MVN_i}(t) = \lambda_3 \cdot \int_{-\infty}^{+\infty} k_2 \left(\frac{t - t_{PC_{spike}}}{\sigma_{MF-MVN}} \right) \cdot \delta_{MF_{spike}}(t) \cdot dt$$

$$\quad \text{if } PC_j \text{ is active at } t$$

$$LTP. \Delta w_{MF_j-MVN_i}(t) = \lambda_4 \cdot \delta_{MF_{spike}}(t) \quad const. \quad otherwise$$

$$(26)$$

with $\Delta W_{MF_j-MVN_i(t)}$ denoting the weight change between the jth MF and the target ith MVN. $\sigma_{MF-DCN} = 5$ ms standing for the temporal width of the kernel; δ_{MF} representing the Dirac delta function that defines a MF spike. $\lambda_3 = -0.0512$ nS is the synaptic efficacy decrement whereas $\lambda_4 = 0.00132$ nS is the synaptic efficacy increment. Finally, the integrative kernel function $k_2(x)$ is defined as Eq. (27) (Luque et al., 2016):

$$k_2(x) = e^{-|x|} \cdot \cos(x)^2 \tag{27}$$

Note that there is compensation of the sensory–motor pathway delay at this site since it has already been done at the PF–PC synapses (τ_{LTD} in Eq. (24)). The STDP rule defined by Eq. (26) produces a synaptic efficacy decrease (LTD) when a spike from the PC reaches the target MVN neuron. The amount of synaptic decrement (LTD) depends on the activity which arrives through the MFs. This activity is convolved with the kernel defined in Eq. (27). This LTD mechanism computes on those MF spikes arriving after/before the PC spike arrival within the time window defined by the kernel. The amount of LTP at the MF–MVN synapses is fixed (Ito, 1982; Lev-Ram et al., 2003; Luque et al., 2011a) with an increase in synaptic efficacy, each time a spike arrives through an MF to the target MVN.

The article source code implemented in EDLUT is available at the URL: https://www.ugr.es/~nluque/code_open/CODE_EC_regulated_GABA_Olivary_VOR.rar

4.8. VOR mechanical circuitry

The cerebellum works as a biological controller at the core of a feed-forward control loop. The cerebellar adaptive output from the MVN is driven through a mechanical pathway consisting of a set of motor neurons, nerve fibres and muscles that finally operates the eye. This VOR mechanical pathway was modelled within EDLUT as a continuous-time mathematical model with two poles (Eq. (28)) (Luque et al., 2022):

$$e(kT), E(s) : eye\ motion\ (output)$$

$$h(kT), H(s) : head\ motion\ (input)$$

$$(28)$$

$$VOR(s) = \frac{E(s)}{H(s)} = \frac{k \cdot T_{C1} \cdot s}{(T_{C1} \cdot s + 1) \cdot (T_{C2} \cdot s + 1)} \cdot e^{-s\tau_{delay}}$$

where τ_{delay} (~5 ms) defines the travel delay of the signals from the inner ear to the brain and eyes; K (~0.6) weights the mismatch between the eyes and head movement; T_{C1} ranging [10–30 s] mainly accounts for the dynamics of the semi-circular

canals; T_{C2} ranging [0.005–0.05 s] mainly accounts for the oculomotor dynamics (Robinson, 1981; Skavenski & Robinson, 1973). The VOR temporal response is calculated by applying the inverse Laplace transform to Eq. (28) (Luque et al., 2022), thus obtaining Eqs. (29), (30) (note that the delay was fused within the sensory–motor delay).

$$\begin{bmatrix} \dot{x}_1 \\ \dot{x}_2 \end{bmatrix} = \begin{bmatrix} 0 & 1 \\ -a_0 & -a_1 \end{bmatrix} \cdot \begin{bmatrix} x_1 \\ x_2 \end{bmatrix} + \begin{bmatrix} 0 \\ h(t) \end{bmatrix} \tag{29}$$

$$y = \begin{bmatrix} b_0 & b_1 \end{bmatrix} \cdot \begin{bmatrix} x_1 \\ x_2 \end{bmatrix} \tag{30}$$

where:

$$a_0 = \frac{1}{T_{C1} \cdot T_{C2}}; \, a_1 = \frac{(T_{C1} + T_{C2})}{T_{C1} \cdot T_{C2}}; \, b_0 = 0; \, b_1 = \frac{k \cdot T_{C1}}{T_{C1} \cdot T_{C2}}$$

These VOR mechanical model parameters were obtained using a genetic algorithm to fit experimental and clinical observations (Gordon et al., 1989; Robinson, 1981; Skavenski & Robinson, 1973) as in Luque et al. (2022) obtaining $k = 1.0$, $T_{C1} = 15$, and $T_{C2} = 0.05$.

4.9. The sensory–motor and NO delays

The sensory–motor delay (100 ms) (Sargolzaei et al., 2016) was modelled using two 50 ms circular temporal buffers with 2 ms taps. The first 50 ms circular buffer was located between the cerebellar output and the VOR plant, whereas the second 50 ms circular buffer was located between VOR plant output and the error signal used as cerebellar teaching signal (Eqs. (31), (32)).

$$VOR\_plant_{input} = MVN_{output} \, (t + \delta_1) \tag{31}$$

$$VOR\_plant_{output} = y \, (t + \delta_2) \tag{32}$$

where MVN_{output} defines the analogue cerebellar output Eq. (9) and $\delta_1 = \delta_2 = 50$ ms the delay inserted. y is defined in Eq. (30) as the analogue VOR plant output that is now delayed. Conversely the NO delay was implemented within the EDLUT simulator (Naveros et al., 2017, 2015). The EDLUT simulator can associate a propagation delay structure to each synaptic connection between two neurons (source neuron–target neuron) through which the spike elicited by the source neuron can be delayed in its travel to the target neuron (time propagation). The NO delay was implemented using this EDLUT propagation delay structure (100 ms).

CRediT authorship contribution statement

Niceto R. Luque: Conceived the article initial idea, Designed, modelled and implemented the set-up experimentation, Prepared the figures, Drafted the manuscript, Reviewed the manuscript and approved the final version. **Francisco Naveros:** Designed, modelled and implemented the set-up experimentation, Reviewed the manuscript and approved the final version. **Ignacio Abadía:** Designed, modelled and implemented the set-up experimentation, Prepared the figures, Drafted the manuscript, Reviewed the manuscript and approved the final version. **Eduardo Ros:** Drafted the manuscript, Reviewed the manuscript and approved the final version. **Angelo Arleo:** Conceived the article initial idea, Drafted the manuscript, Reviewed the manuscript and approved the final version.

Declaration of competing interest

The authors declare that they have no known competing financial interests or personal relationships that could have appeared to influence the work reported in this paper.

Appendix A. Supplementary data

Supplementary material related to this article can be found online at https://doi.org/10.1016/j.neunet.2022.08.020.

References

Apps, R., & Hawkes, R. (2009). Cerebellar cortical organization: a one-map hypothesis. *Nature Review of Neuroscience, 10*, 670.

Badura, A., Clopath, C., Schonewille, M., & De Zeeuw, C. I. (2016). Modeled changes of cerebellar activity in mutant mice are predictive of their learning impairments. *Scientific Reports, 6*, 36131.

Barmack, N. H., Fredette, B. J., & Mugnaini, E. (1998). Parasolitary nucleus: a source of gabaergic vestibular information to the inferior olive of rat and rabbit. *Journal of Computational Neurology, 392*, 352–372.

Baumel, Y., Jacobson, G. A., & Cohen, D. (2009). Implications of functional anatomy on information processing in the deep cerebellar nuclei. *Rebuilding Cerebellar Network Computations from Cellular Neurophysiology*.

Belmeguenai, A., Botta, P., Weber, J. T., Carta, M., De Ruiter, M., De Zeeuw, C. I., Valenzuela, C. F., & Hansel, C. (2008). Alcohol impairs LTD at the cerebellar parallel fiber–purkinje cell synapse. *Journal of the Neurophysiology, 100*, 3167–3174.

Bengtsson, F., & Hesslow, G. (2006). Cerebellar control of the inferior olive. *The Cerebellum, 5*, 7.

Best, A. R., & Regehr, W. G. (2009). Inhibitory regulation of electrically coupled neurons in the inferior olive is mediated by asynchronous release of GABA. *Neuron, 62*, 555–565.

Carey, M. R., & Regehr, W. G. (2009). Noradrenergic control of associative synaptic plasticity by selective modulation of instructive signals. *Neuron, 62*, 112–122.

Carrillo, R. R., Ros, E., Boucheny, C., & Coenen, O. (2008). A real-time spiking cerebellum model for learning robot control. *Biosystems, 94*, 18–27.

Clopath, C., Badura, A., De Zeeuw, C. I., & Brunel, N. (2014). A cerebellar learning model of VOR adaptation in wild-type and mutant mice. *Journal of the Neuroscience, 34*, 7203–7215.

De Zeeuw, C. I., Hoogenraad, C. C., Koekkoek, S. K. E., Ruigrok, T. J., Galjart, N., & Simpson, J. I. (1998). Microcircuitry and function of the inferior olive. *Trends in Neurosciences, 21*(9), 391–400.

De Zeeuw, C., Van, A. A., Hawkins, R., & Ruigrok, T. (1997). Climbing fibre collaterals contact neurons in the cerebellar nuclei that provide a gabaergic feedback to the inferior olive. *Neuroscience, 80*, 981–986.

Devor, A., & Yarom, Y. (2002). Generation and propagation of subthreshold waves in a network of inferior olivary neurons. *Journal of the Neurophysiology, 87*, 3059–3069.

Eccles, J. C., Ito, M., & Szentágothai, J. (1967). *The cerebellum as a neuronal machine (Vol. 53)*. New York: Springer-Verlag.

Gerstner, W., & Kistler, W. M. (2002). *Spiking neuron models: single neurons, populations, plasticity*. Cambridge University Press.

Gordon, J. L., Furman, J. M. R., & Kamen, E. W. (1989). System identification of the vestibulo-ocular reflex: application of the recursive least-squares algorithm. In *Bioengineering conference, 1989. Proceedings of the 1989 fifteenth annual northeast* (pp. 199–200). IEEE.

He, Q., Titley, H., Grasselli, G., Piochon, C., & Hansel, C. (2013). Ethanol affects NMDA receptor signaling at climbing fiber-purkinje cell synapses in mice and impairs cerebellar LTD. *Journal of the Neurophysiology, 109*, 1333–1342.

Hesslow, G. (1986). Inhibition of inferior olivary transmission by mesencephalic stimulation in the cat. *Neuroscience Letters, 63*, 76–80.

Hoge, G. J., Davidson, K. G. V., Yasumura, T., Castillo, P. E., Rash, J. E., & Pereda, A. E. (2011). The extent and strength of electrical coupling between inferior olivary neurons is heterogeneous. *Journal of the Neurophysiology, 105*, 1089–1101.

Honda, T., Yamazaki, T., Tanaka, S., Nagao, S., & Nishino, T. (2011). Stimulus-dependent state transition between synchronized oscillation and randomly repetitive burst in a model cerebellar granular layer. *PLOS Computational Biology*, 7, Article e1002087.

Ito, M. (1982). Cerebellar control of the VOR; around the flocculus hypothesis. *Annual Review of Neuroscience*, 5, 275–297.

Ito, M. (1984). The cerebellum and neural control.

Ito, M. (2001). Cerebellar long-term depression, characterizations, signal transduction and functional roles. *Physiological Review*, 81, 1143–1195.

Ito, M. (2002). The molecular organization of cerebellar long-term depression. *Nature Reviews Neuroscience*, 3, 896.

Kawato, M., & Gomi, H. (1992). A computational model of four regions of the cerebellum based on FEL. *Biological Cybernetics*, 68, 95–103.

Kawato, M., Kuroda, S., & Schweighofer, N. (2011). Cerebellar supervised learning revisited: biophysical modeling and degrees-of-freedom control. *Current Opinion in Neurobiology*, 21, 791–800.

Kettner, R. E., Mahamud, S., Leung, H., Sittko, N., Houk, J. C., Peterson, B. W., & Barto, A. G. (1997). Prediction of complex two-dimensional trajectories by a cerebellar model of smooth pursuit eye movement. *Journal of the Neurophysiology*, 77, 2115–2130.

Latorre, R., Aguirre, C., Rabinovich, M. I., & Varona, P. (2013). Transient dynamics and rhythm coordination of inferior olive spatio-temporal patterns. *Frontiers on Neural Circuits*, 7, 1–18.

Lefler, Y., Yarom, Y., & Uusisaari, M. Y. (2014). Cerebellar inhibitory input to the inferior olive decreases electrical coupling and blocks subthreshold oscillations. *Neuron*, 81, 1389–1400.

Leigh, R. J., & Zee, D. S. (2015). *The neurology of eye movements*. Oxford University Press.

Lev-Ram, V., Meht, S. B., Kleinfeld, D., & Tsien, R. Y. (2003). Reversing cerebellar long term depression. *Proceedings of the National Academy of Sciences of the United States of America*, 100, 15989–15993.

Li, C., Han, L., Ma, C.-W., Lai, S.-K., Lai, C.-H., Shum, D. K. Y., & Chan, Y.-S. (2013). Maturation profile of inferior olivary neurons expressing ionotropic glutamate receptors in rats: role in coding linear accelerations. *Brain Structure and Function*, 218, 833–850.

Llinas, R., Baker, R., & Sotelo, C. (1974). Electrotonic coupling between neurons in cat inferior olive. *Journal of the Neurophysiology*, 37, 560–571.

Longley, M., & Yeo, C. H. (2014). Chapter 4 - Distribution of neural plasticity in cerebellum-dependent motor learning. In N. Ramnani (Ed.), *Progress in brain research, Vol. 210* (pp. 79–101). Elsevier.

Lorente de Nó, R. (1933). Vestibulo-ocular reflex arc. *Archive Neurology & Psychiatry*.

Luque, N. R., Garrido, J. A., Carrillo, R. R., Coenen, O.-J. M.-D., & Ros, E. (2011a). Cerebellar input configuration toward object model abstraction in manipulation tasks. *IEEE Transactions on Neural Networks*, 22, 1321–1328.

Luque, N. R., Garrido, J. A., Carrillo, R. R., Coenen, O.-J. M.-D., & Ros, E. (2011b). Cerebellarlike corrective model inference engine for manipulation tasks. *IEEE Transactions on Systems, Man and Cybernetics*, 41, 1299–1312.

Luque, N. R., Garrido, J. A., Carrillo, R. R., D'Angelo, E., & Ros, E. (2014). Fast convergence of learning requires plasticity between inferior olive and deep cerebellar nuclei in a manipulation task: a closed-loop robotic simulation. *Frontier on Computers Neuroscience*, 8.

Luque, N. R., Garrido, J. A., Naveros, F., Carrillo, R. R., D'Angelo, E., & Ros, E. (2016). Distributed cerebellar motor learning; a STDP model. *Frontier on Computers Neuroscience*, 10.

Luque, N. R., Naveros, F., Carrillo, R. R., Ros, E., & Arleo, A. (2019). Spike burst-pause dynamics of purkinje cells regulate sensorimotor adaptation. *PLoS Computational Biology*, 15, Article e1006298.

Luque, N. R., Naveros, F., Sheynikhovich, D., Ros, E., & Arleo, A. (2022). Computational epidemiology study of homeostatic compensation during sensorimotor aging. *Neural Networks*, 146, 316–333.

Marshall, S. P., & Lang, E. J. (2009). Local changes in the excitability of the cerebellar cortex produce spatially restricted changes in complex spike synchrony. *Journal of Neuroscience*, 29, 14352–14362.

Medina, J., & Mauk, M. (1999). Simulations of cerebellar motor learning: computational analysis of plasticity at the mossy fiber synapse. *Journal of the Neuroscience*, 19, 7140–7151.

Medina, J. F., & Mauk, M. D. (2000). Computer simulation of cerebellar information processing. *Nature Neuroscience*, 3, 1205–1211.

Minor, L. B., & Goldberg, J. M. (1991). Vestibular-nerve inputs to the VOR a functional-ablation study in the squirrel monkey. *Journal of the Neuroscience*, 11, 1636–1648.

Najac, M., & Raman, I. M. (2015). Integration of Purkinje cell inhibition by cerebellar Nucleo-Olivary neurons. *Journal of the Neuroscience*, 35, 544–549.

Najac, M., & Raman, I. M. (2017). Synaptic excitation by climbing fibre collaterals in the cerebellar nuclei of juvenile and adult mice. *Journal Physiology*, 595, 6703–6718.

Najafi, F., & Medina, J. F. (2013). Beyond all-or-nothing climbing fibers: graded representation of teaching signals in Purkinje cells. *Frontier on Neural Circuits*, 7, 1–15.

Naveros, F., Garrido, J. A., Carrillo, R. R., Ros, E., & Luque, N. R. (2017). Event-and time-driven techniques using parallel CPU–GPU co-processing for spiking neural networks. *Frontiers on Neuroinformatics*, 11.

Naveros, F., Luque, N. R., Garrido, J. A., Carrillo, R. R., Anguita, M., & Ros, E. (2015). A spiking neural simulator integrating event-driven and time-driven computation schemes using parallel CPU–GPU co-processing: A case study. *IEEE Transactions on Neural Networks and Learning Systems*, 26, 1567–1574.

Nobukawa, S., & Nishimura, H. (2016). Chaotic resonance in coupled inferior olive neurons with the Llinás approach neuron model. *Neural Computation*, 28, 2505–2532.

Pickford, J., & Apps, R. (2017). Collateral impact: a dual role for climbing fibre collaterals to the cerebellar nuclei? *Journal Physiology*, 595, 6589.

Rambold, H., Churchland, A., Selig, Y., Jasmin, L., & Lisberger, S. G. (2002). Partial ablations of the flocculus and ventral paraflocculus in monkeys cause linked deficits in smooth pursuit eye movements and adaptive modification of the VOR. *Journal of the Neurophysiology*, 87, 912–924.

Raymond, J. L., & Lisberger, S. G. (1998). Neural learning rules for the vestibulo-ocular reflex. *Journal of the Neuroscience*, 18, 9112–9129.

Robinson, D. A. (1981). The use of control systems analysis in the neurophysiology of eye movements. *Annual Review of Neuroscience*, 4, 463–503.

Ros, E., Carrillo, R. R., Ortigosa, E. M., Barbour, B., & Agís, R. (2006). Event-driven simulation scheme for spiking neural networks using lookup tables to characterize neuronal dynamics. *Neural Computation*, 18, 2959–2993.

Sargolzaei, A., Abdelghani, M., Yen, K. K., & Sargolzaei, S. (2016). Sensorimotor control: computing the immediate future from the delayed present. *BMC Bioinformatics*, 17, 501–509.

Schneidman, E. (2016). Towards the design principles of neural population codes. *Current Opinion in Neurobiology*, 37, 133–140.

Schweighofer, N., Doya, K., Fukai, H., Chiron, J. V., Furukawa, T., & Kawato, M. (2004). Chaos may enhance information transmission in the inferior olive. *Proceedings of the National Academy of Sciences of the United States of America*, 101, 4655–4660.

Schweighofer, N., Doya, K., & Kawato, M. (1999). Electrophysiological properties of inferior olive neurons: a compartment model. *Journal of the Neurophysiology*, 82, 804–817.

Skavenski, A. A., & Robinson, D. A. (1973). Role of abducens neurons in vestibuloocular reflex. *Journal of Neurophysiology*, 36, 724–738.

Stollnitz, E. J., DeRose, T. D., & Salesin, D. H. (1996). *Wavelets for computer graphics: theory and applications*. Morgan Kaufmann.

Stone, L. S., & Lisberger, S. G. (1990). Visual responses of purkinje cells in the cerebellar flocculus during smooth-pursuit eye movements in monkeys, I. Simple spikes. *Journal of the Neurophysiology*, 63, 1241–1261.

Suvrathan, A., Payne, H. L., & Raymond, J. L. (2016). Timing rules for synaptic plasticity matched to behavioral function. *Neuron*, 92, 959–967.

Svensson, P., Bengtsson, F., & Hesslow, G. (2006). Cerebellar inhibition of inferior olivary transmission in the decerebrate ferret. *Experimental Brain Research*, 168, 241–253.

Tokuda, I. T., Hoang, H., & Kawato, M. (2017). New insights into olivo-cerebellar circuits for learning from a small training sample. *Current Opinion in Neurobiology*, 46, 58–67.

Tokuda, I. T., Hoang, H., Schweighofer, N., & Kawato, M. (2013). Adaptive coupling of inferior olive neurons in cerebellar learning. *Neural Networks*, 47, 42–50.

Turecek, J., & Regehr, W. G. (2020). Cerebellar and vestibular nuclear synapses in the inferior olive have distinct release kinetics and neurotransmitters. *Elife*, 9, Article e61672.

Turrigiano, G. G., & Nelson, S. B. (2004). Homeostatic plasticity in the developing nervous system. *Nature Review in Neuroscience*, 5, 97–107.

Uusisaari, M., & De Schutter, E. (2011). The mysterious microcircuitry of the cerebellar nuclei. *Journal Physiology*, 589, 3441–3457.

Van Alphen, A. M., Stahl, J. S., & De Zeeuw, C. I. (2001). The dynamic characteristics of the mouse horizontal vestibulo-ocular and optokinetic response. *Brain Research*, 890, 296–305.

Voogd, J., & Glickstein, M. (1998). The anatomy of the cerebellum. *Trends on Neuroscience*, 21, 370–375.

Wang, X.-J., & Buzsáki, G. (1996). Gamma oscillation by synaptic inhibition in a hippocampal interneuronal network model. *Journal of the Neuroscience*, 16, 6402–6413.

Williams, J. A., Bridgeman, B., Woods, T., & Welch, R. (2007). Global VOR gain adaptation during near fixation to foveal targets. *Human Movement Science*, 26, 787–795.

Yamazaki, T., & Tanaka, S. (2005). Neural modeling of an internal clock. *Neural Computation*, 17, 1032–1058.

Yamazaki, T., & Tanaka, S. (2007). The cerebellum as a liquid state machine. *Neural Networks*, 20, 290–297.

Yamazaki, T., & Tanaka, S. (2009). Computational models of timing mechanisms in the cerebellar granular layer. *Cerebellum*, 8, 423–432.